UCLouvain

epl

École polytechnique de Louvain

Design and Prevalidation of a Bio-Inspired Musculoskeletal Model of a Bird

Level Flapping Flight

Author: **Lorenzo Barbuscia**
Supervisor: **Renaud Ronsse**
Readers: **Philippe Chatelain, Victor Colognesi, Nicolas Docquier, Paul Fisette**
Academic year 2020–2021
Master [120] in Mechanical Engineering

Acknowledgments

First of all, I would like to express my gratitude to my promoter, **Prof. Renaud Ronsse** for his help. He guided me in the writing of this work and gave me good advice for the path to take in the elaboration of the modelisation. Thank you for your involvement, your patience and your support.

I'm extremely grateful to the **Meed** division of the IMMC and especially the **Robotran teams**. Their help to find appropriate methodology was really precious.

I would also like to thank **Mr. Victor Colognesi** who accompanied me for aerodynamic aspect and gave me insights about the flight kinematic.

Thank you also to **all the persons** involved in one way or another who helped me for the improvement of my work, who enabled me to carry out this master thesis.

Last but not least, I would like to express my gratitude to my **friends** who supported and encouraged me during these long months of studies. I would like to thank my **family** for their support and for their endless love .

Abstract

This master thesis proposes a multiphysics framework coupling biomechanics and aerodynamics for the simulation of bird flight. It presents a biomechanical model based on the anatomy of a bird, which models the wing by articulated segments. It develops a bio-inspired model for locomotion in flapping flight. The present work is devoted, on the one hand, to review, select, adapt, improve, develop and validate methods and tools necessary for this model: build a multi-body model of a bird, characterize the properties of the skeleton and the musculoskeletal system, evaluate the aerodynamic forces, actuate the skeleton in a bio-inspired way, estimate the energetic cost, evaluate and study the kinematics of flight. And, on the other hand, to apply them to a bird of interest (i.e. the Northern Bald Ibis). We describe the key parameters that mark the development of such a musculoskeletal model. We intend to provide the necessary milestones with particular accent on the methodology related to the musculoskeletal model.

We chose a modular approach to break down the overall goal into smaller modules. While being able to modify or improve a single module without affecting the rest. Each module contains its own library of sub-functions dedicated to their domain. These modules work together and are organized around the Robotran program.

Contents

List of Figures

List of abbreviations

The next list describes several symbols that will be later used within the body of this master thesis

$\hat{X}_e$	Earth frame
$\hat{X}_b$	Body frame
$\hat{X}_p^S$	Wing S section p frame
Ψ	Yaw angle
Θ	Pitch angle
Φ	Roll angle
$\vec{r}_{ori}$	Locations of the muscle origin in the distal bones (i.e. distal attachment segment) local frame
$\vec{r}_{ins}$	Locations of the muscle insertion in the distal bones (i.e. distal attachment segment) local frame
$\vec{R}_{ori}$	Locations of the muscle origin in the proximal bones (i.e. proximal attachment segment) local frame
F_{mtu}	Musculotendon force
$\vec{u}_{mtu}$	Unit vector of the muscle line of action
$\vec{\mathcal{T}}_{mtu}$	Joint torques driven by muscles
$\vec{r}_{mtu}$	Muscular moment arm
$\underline{\underline{J}}$	Jacobian matrix of muscular moment arms
c_1	Root chord of the wing
c_2	Proximal intermediate chord of the wing
c_3	Distal intermediate chord of the wing

c_4 Tip chord of the wing

l_A Length of the arm

l_F Length of the forearm

l_H Length of the hand segment

$\underline{q}$ Vector of coordinates

$\hat{X}_w$ Wind frame

$\vec{V}_{rel}$ Velocity vector of the bird relative to the air

T_{flight} Flight period i.e. time of a flapping flight cycle

D_{body} Bird's body drag force

$C_{d,body}$ Drag coefficient of the body

ρ_{air} Air density

S_b Frontal surface of the body

m_{bird} Mass of the bird

A_b Equivalent flat plate of the body area

S_w Wing disc area whose diameter is equal to the wing span

MTU Muscle tendon unit

CNS Central nervous system

a_m Muscular activation

s_m Neural stimulation

F_m Muscle force

F_t Tendon force

l_{mtu} Musculotendon length

l_m Muscle length

l_t Tendon length

v_m, $\dot{l_m}$ Muscle velocity

v_{mtu}, $\dot{l_{mtu}}$ Musculotendon velocity

α Pennation angle

l_m^{α} Effective muscle length with pennation

CE Active contractile element

PE Passive parallel elastic element

BE Passive buffer elastic element

SE Passive serial elastic elemen

l_{ce} CE length

l_{se} SE length

l_{opt} Optimal length of the muscle

l_{min} Minimal length of the muscle

l_{slack} Slack length of the tendon

PCSA Physiological cross-section area of the muscle

F_m^{iso} Maximum isometric force of the muscle

v_{max} Maximum shortening velocity of the muscle at null load

w_t Muscle thickness

t_s Muscle time-scaling parameter

α_0 Optimal pennation angle of the muscle fiber

$\widetilde{v_{max}}$ Normalised maximum shortening velocity

$\widetilde{l_{slack}}$ Dimensionless slack length of the tendon

f_m Dimensionless muscle force

f_t Dimensionless tendon force

f_{ce} Dimensionless force of CE

f_{se} Dimensionless force of SE

f_{pe} Dimensionless force of PE

f_{be} Dimensionless force of BE

$\widetilde{l_{ce}}$ Dimensionless length of CE

$\widetilde{\dot{l}_{ce}}$ Dimensionless shortening velocity of CE

τ Dimensionless time of the muscle

f_l Force-length relationship of CE

f_v Force-velocity relationship of the muscle

f_{pe}^{*} Force-length relationship of PE

ε_{CE} Strain of CE

ε_{BE} Strain of BE

ε_{SE} Strain of SE

f_{m}^{*} Static muscle force

k_t Absolute tendon stiffness

$\widetilde{k_t}$ Dimensionless absolute tendon stiffness

$\dot{\mathcal{H}}$ Rate of muscle heat production

$\mathcal{P}$, $\dot{\mathcal{W}}$ Muscle power or rate of muscle work

$\widetilde{\dot{l}_{ce}^{opt}}$ Dimensionless shortening velocity of CE at which the peak of power occurs

$\dot{\mathcal{E}}$ Total rate of metabolic energy consumption

$\mathcal{P}_{ce}$ Power of CE

$\widetilde{p_{ce}}$ Dimensionless power of CE

f_{v}^{opt} Dimensionless optimal load at which the peak of power occurs

f_{v}^{opt} Dimensionless load at which the peak of power occurs

$\mathcal{P}_{ce}^{opt}$ Power peak of CE

PT Muscle pectoralis

SC Muscle supracoracoideus

SHC Muscle scapulohumeralis caudalis

CBC Muscle coracobrachialis caudalis

TH Muscle triceps brachii humeral head

BB Muscle biceps brachii

TP Muscle tensor propatagialis

EMR Muscle extensor metacarpi radialis

FCU Muscle flexor carpi ulnaris

ECU Muscle extensor carpi ulnaris

m_{mtu} Muscle mass

l_{belly} Belly length of the muscle

ρ_m Muscle density

σ_{iso}^{m} Isometric stress under maximal activation

GP Golden Pheasant (Chrysolophus pictus)

NBI Northern Bald Ibis (Geronticus eremita)

α_0^{max} Maximum possible optimal pennation angle

α_0^{neg} negligible optimal pennation angle

t_{act} muscle activation time constant when muscle is fully excited

t_{deact} muscle activation time constant when muscle is unexcited

τ_{act} Dimensionless activation time constant when muscle is fully excited

τ_{deact} Dimensionless activation time constant when muscle is unexcited

τ_{mtu} Dimensionless musculotendon time

$\dot{a_m}$ Muscle activation derivative

EC Excitation-contraction (

β Ratio between the activation and deactivation time constants of the muscle

f_{act} Muscle activation frequency

l_{ce}^{*} Static length of CE or length of CE at steady state

CHAPTER 1

Introduction

Historically, from Leonardo da Vinci to many others and through the ages, man has never ceased to look to the sky and marvel at the fascinating spectacle of birds. Who has never watched the birds during their incessant ballet when spring comes. They are sometimes alone, sometimes in groups, some of them are small, while others are nocturnal, some are fast and some are even migratory. There are so many aspects and parameters that nature has already tried out, improved and perfected over time. Of course, today there are airplanes and this is still a tremendous technical feat. It is already an achievement but not an end in itself. We can do better and push the limits of our understanding of flight locomotion. We know that nature is not only a source of raw materials but also of innovation and inspiration. For many things it is still the best in terms of weight, efficiency and energy consumption. This thesis is in a direction of learning from nature. Indeed, this thesis is at the crossroads of biomechanics, fluid mechanics and control with the aim of mimicking nature. And more precisely, the kinematics of bird's flapping flight. Because we need to do more to reduce fuel consumption, etc.

This master thesis will focus on the methodology and approaches used in the development of a neuromusculoskeletal model and its formalism in order to provide a reliable framework for future research and applications.

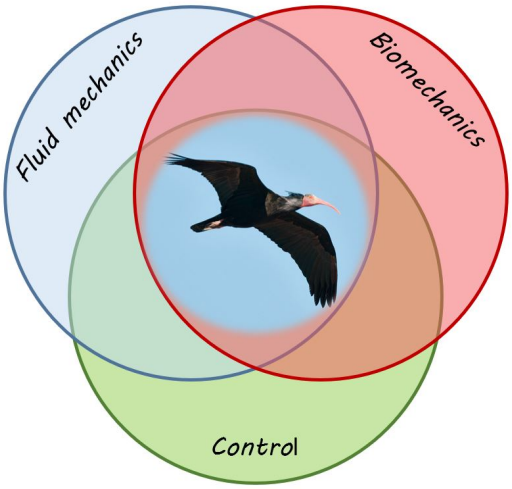

Figure 1.1: The picture of the Northern Bald Ibis in the center was taken by Leander Khil on Tamri (Morocco), 2012

1.1 Context and motivation

The ecological footprint remains a major issue for the airline industry. Researchers at UCLouvain propose to take inspiration from the flight of migratory birds to reduce fuel consumption. Migratory birds flying in a V formation flock are able to travel several thousand kilometers, while saving energy. Just like migratory birds, airplanes should be able to benefit from the wake of other airplanes to reduce their energy consumption.

With 25 years of expertise in the study of aircraft wakes, formation flights are studied at the Institute of Mechanics, Materials and Civil Engineering (IMMC) at UCLouvain. The follower bird comes to exploit the wakes of the predecessor when it is at its strongest. This can work very well for aircraft. Because aircraft vortices are straight. They are not oscillating like the bird's vortices and are therefore even easier to exploit. Well positioned in the wake of its predecessor, a follower aircraft could save 5 to 10 % of its fuel consumption. For comparison, such gains are equivalent to 10 to 20 years of research and development to create new engines or new aircraft shapes to reduce fuel consumption. This is particularly interesting on long flights. The aircrafts will synchronise to fly together for a good part of the flight until they separate and fly to their final destination.

Researchers at UCLouvain have developed onboard intelligence algorithms that can be installed on an aircraft's onboard computer so that it can sense the wake of a predecessor (Figure 1.2). The airplane will then adapt its trajectory to better position itself with respect to this wake. While avoids entering the dangerous zone created by the wakes. They try to reproduce the sensorial apparatus of the bird which has feathers with nerves, tendons and muscles.

Figure 1.2: Simulation of an aircraft in the wake of a leader [1]

Migratory birds achieve tremendous energy savings by flying in so-called V formations, which allows most of them to benefit from upwash generated by their predecessor. A core question is to determine how these optimised formations emerge. The study of bird flight, and more particularly of migratory birds, is at the heart of the RevealFlight project at UCLouvain in which Professor Philippe Chatelain, a specialist in fluid mechanics, collaborates with Professor Renaud Ronsse, a specialist in biomechanics and Professor

Julien Hendrickx, a specialist in mathematical engineering.

The RevealFlight project is a multi-disciplinary project ("*shedding light on the efficiency optimization mechanisms deployed by biological flyers*", `https://sites.uclouvain.be/RevealFlight/`). This framework aims at investigating the mechanisms characterising biological flyers, at the scale of migratory birds, and mainly builds upon fives topics:

- Biological models: Development of a musculoskeletal model with enough resolution, to capture locomotive functions, and a neuronal model governing muscle activation and gait coordination.
- Body dynamics: Interaction between the flyer and the flow, aimed at assessing the stability, and investigating about the bio-inspired control scheme for flapping flight.
- Fluid mechanics: Evaluation of the aerodynamic forces on the bird wing with different levels of accuracy (potential flow, unsteady lifting line and CFD methods).
- Learning and optimisation: Reinforcement Learning approach to train the flyer in maneuvers and wake exploitation scenarios.
- Agent models: the flyer is identified as an Agent, endowed with decision, action capability, and social interactions.

This master thesis will take place within this multi-disciplinary project. The goal of this thesis is to develop a bio-inspired model for flapping flight locomotion.

We will model and analyse a bird, the numerical values used in the simulations are those of the bird of interest in the RevealFlight project, i.e. the Northern Bald Ibis (Geronticus eremita). It is fundamental to establish the right level of abstraction of the model, in order to converge to a model with a complexity level corresponding to the investigated hypotheses. Such a model should, for example, allow the calculation of energy consumption during the flight. Because this kind of data can not be obtained experimentally (as in the case of humans by the oxygen survey, lung measurements, etc).

Therefore, the present work is devoted, on one hand, to review, select, adapt, improve, develop and validate all the necessary methods and tools which are required for this purpose:

- Build a multi-body model of a bird.
- Characterize the properties of the skeleton and the musculoskeletal system.
- method for evaluating aerodynamic forces.
- method for actuating the skeleton in a bio-inspired manner
- method for energetic cost estimation.
- method to evaluate and study the flight kinematics.

And, on the other hand, to apply them to the bird of interest.

We chose a modular approach to break down the overall goal into smaller modules. While being able to modify or improve a single module without affecting the rest. Each module contains its own library of sub-functions dedicated to their domain. These modules work together and are organized around the Robotran program.

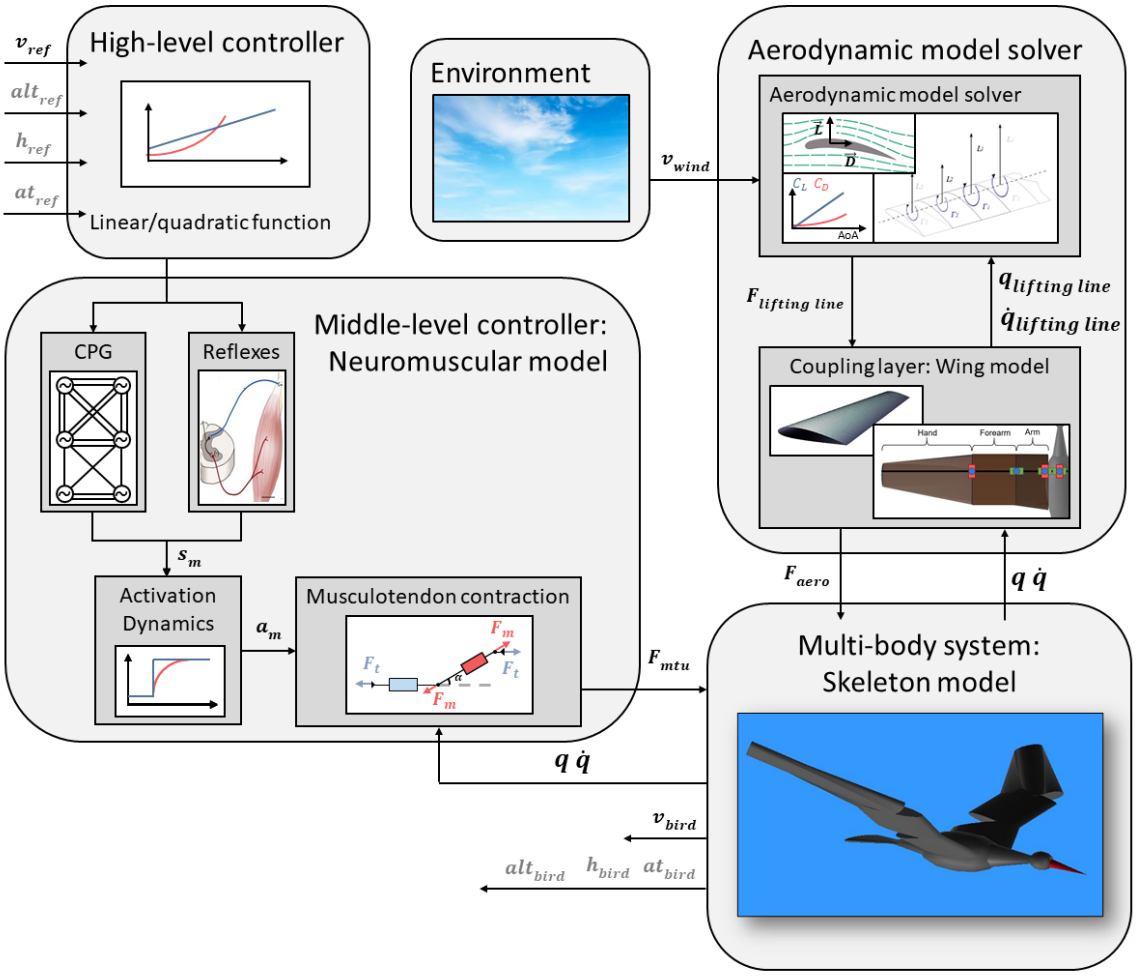

Figure 1.3: The controller final purpose is to compute the appropriate internal forces to actuate the multi-body system (and make the bird flight). The controller is divided into two parts: (i) the high-level controller provides commands to the middle-level controller by modulating key parameters as linear or quadratic functions of four scalar inputs (i.e. the horizontal speed reference v_{ref}, the altitude reference alt_{ref}, the heading reference h_{ref} and the attitude reference at_{ref}), in order to adapt the gait accordingly; (ii) the middle-level controller computes the musculotendon force F_{mtu} (and position references q_{ref} from imposed kinematic), while receiving sensory information from the multi-body system, joint positions q and velocities $\dot{q}$ and key parameters modulated by the high-level controller. Regarding the neuromuscular model, the interplay between the CPG and the reflexes provides stimulation signals s_m. They are later converted into activations a_m controlling the virtual Hill-type muscles. These muscles finally produce forces F_{mtu}, converted to the joint torques via lever arms. In parallel, some position references are computed.

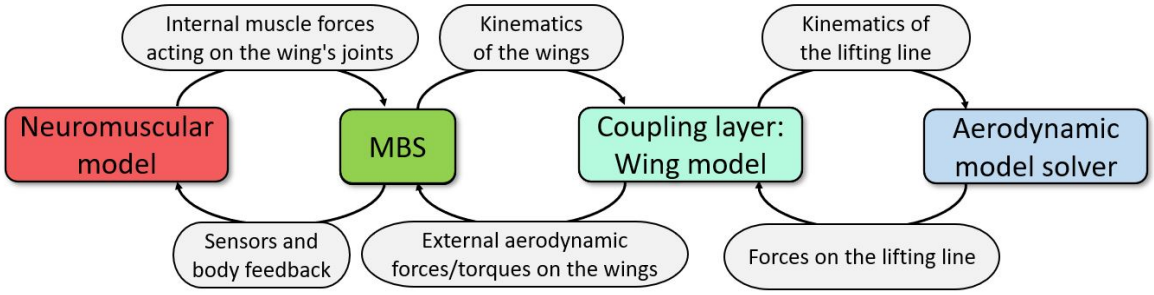

Figure 1.4: Coupling scheme used between the solvers, inspired from [2].

1.2 Master thesis outline

The remainder of this thesis is organized as follows:

- **Chapter 2:** description of the muti-body system of the bird as well as its skeletal model. The musculoskeletal model is also introduces.

- **Chapter 3:** description of a simple aerodynamic model.

- **Chapter 4:** description of the muscle model. In this work, only the skeletal muscles will be discussed. Then when there is a mention to muscle, it refers more specifically to skeletal muscle (or "voluntary muscle").

- **Chapter 5:** description of the level flapping flight through the kinematics of the wing and the aerodynamic forces.

- **Chapter 6:** draws the conclusions and indicates future research lines.

CHAPTER 2

Multi-body and skeletal model

The objective of this chapter is to model and represent the multi-body system of the bird, the skeleton of the wings (i.e bird forelimbs) as well as its articulations. The modeling of the multi-body system of the bird is an imperative step for the calculation of the internal forces generated by the muscles and the external aerodynamic forces. The articulations and their degrees of freedom must also be determined in order to be able to move the skeleton in a consistent way. In addition, during the research, the development of a kinematics for flapping flight, the degrees of freedom of the wings will be limited by a series of physical and biological constraints.

2.1 Multi-body modelling

Before entering into the heart of the subject, we will define the Earth and body reference frames that will be used in this work. We adapt to the bird the conventional axes of fixed-wing aircraft flight dynamics:

Earth frame $\hat{X}_e$:

- $\vec{x_e}$ axis: positive in the direction of north
- $\vec{y_e}$ axis: positive in the direction of east
- $\vec{z_e}$ axis: positive towards the center of the Earth

The Earth frame is assumed to be inertial with a flat $\vec{x_e}$,$\vec{y_e}$-plane. In this frame of reference, the weights are fixed in the positive $\vec{z_e}$ direction.

Body frame $\hat{X}_b$: (illustrated in the Figure 2.1)

- $\vec{x_b}$ axis: positive out the nose of the bird in the plane of symmetry of the bird
- $\vec{z_b}$ axis: perpendicular to the $\vec{x_b}$ axis, in the plane of symmetry of the bird, positive below the bird.
- $\vec{y_b}$ axis: perpendicular to the $\vec{x_b}$,$\vec{z_b}$-plane, positive out the right wing (i.e. determined by the right-hand rule).

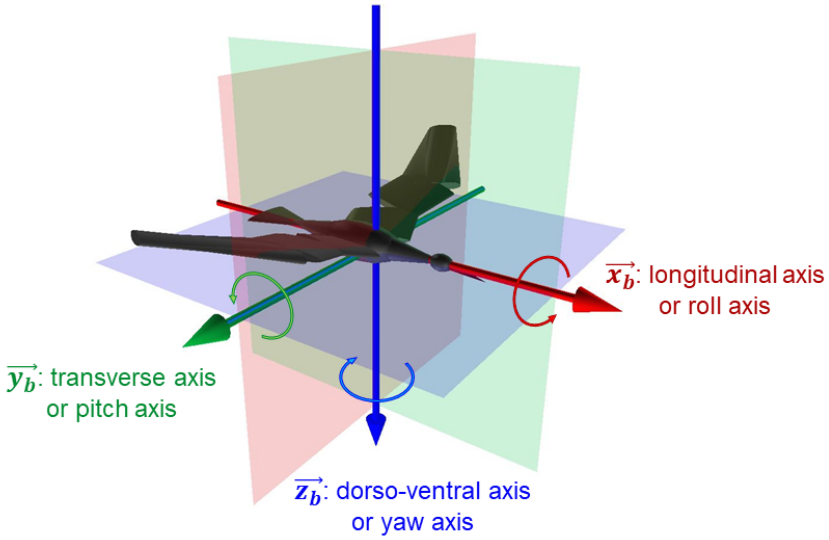

Figure 2.1: Body frame of the bird

The various angles relating the reference frames are explained below. We use the convention of Tait-Bryan angles. It means that the rotation sequences used is z-y'-x". Based on the rotations and axes conventions above:

Tait-Bryan angles from Earth frame to body frame:

- Yaw angle Ψ: azimuth angle, i.e angle between north and the projection of $\vec{x_b}$ onto the horizontal plane ($\vec{x_e}$,$\vec{y_e}$-plane).
- Pitch angle Θ: elevation angle, i.e angle between $\vec{x_b}$ and its projection onto the horizontal plane.
- Roll angle Φ: rotation around $\vec{x_b}$ axis after the yaw and pitch rotation.

To begin multi-body modelling, it is important to start by making a simplified representation of the bird. At this stage it would be counterproductive to go into too much detail and complexity. Therefore, we represent the bird by its two wings and its body. We do not individually model its head, neck, legs nor tail (i.e. they are all part of the main body of the bird). These parts, although important for the bird, have a moderate to low impact on the level flapping flight in compare with the wings. The wing is divided into three sections: the arm, the forearm and the hand (Figure 2.7), which are described in Section 2.1.2. Each section is connected to one or two other sections by joints. The joints are discussed in more detail in Section 2.1.1. Each wing section is modelled as a single rigid body.
Since the wings are split into 3 sections each. These sections have their own reference frame. The exponent R or L indicates if it is the right or left wing. While the subscript a, f or h determines if it is respectively the arm, the forearm or the hand section. These are defined by the body frame and the joint rotation matrices between the section and the main body. For the frame of an arbitrary section and side, we will use the notation section p and side S ($\hat{X}_p^S$).

Wing sections frames:

- Left arm frame: $\vec{x_a^L}, \vec{y_a^L}, \vec{z_a^L}$
- Left forearm frame: $\vec{x_f^L}, \vec{y_f^L}, \vec{z_f^L}$
- Left hand frame: $\vec{x_h^L}, \vec{y_h^L}, \vec{z_h^L}$
- Right arm frame: $\vec{x_a^R}, \vec{y_a^R}, \vec{z_a^R}$
- Right forearm frame: $\vec{x_f^R}, \vec{y_f^R}, \vec{z_f^R}$
- Right hand frame: $\vec{x_h^R}, \vec{y_h^R}, \vec{z_h^R}$

2.1.1 Biological joints and degrees of freedom

Biological joints are different from technical joints (i.e. revolute and prismatic joints). A biological joint is characterised by the contact between 2 surfaces (like wheel-rail contact). For example, look at the shoulder joint in Figure 2.2. It is described by a thoracic surface on which the head of the humerus rotates and moves. It can be modelled by 6 degrees of freedom (DOFs) and the 2 DOFs of the contact point on the thoracic surface. 3 constraints equations are needed to place the head of the humerus on the contact point. In the end, the joint has 5 DOFs. Of course, ligaments and muscles will constrain some of these degrees of freedom.

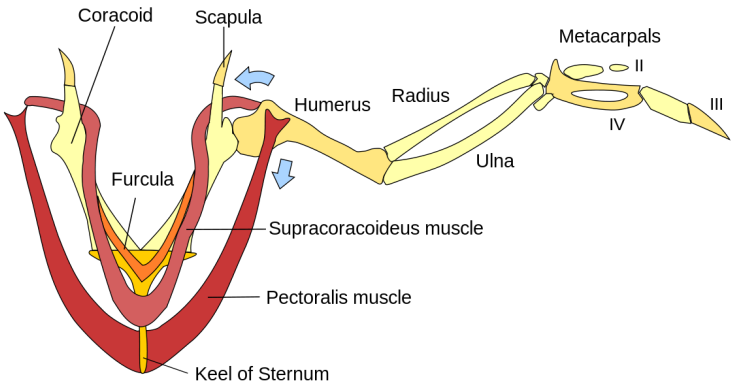

Figure 2.2: Bird's wing anatomy [3]

To achieve such a representation, the shape and size of the contact area must be identified. The adhesion between the two surfaces must be characterised. The tangential and normal forces at the contact surface must be calculated. Without mentioning the effects of elastic deformations of the bodies. Moreover, as each biological joint is unique, it requires a large amount of information on each joint. This kind of representation is completely beyond the scope of this work.

We decided to simply represent the articulations by a series of revolute joints. In regard to the functional movement of the wing (Figure 2.3)

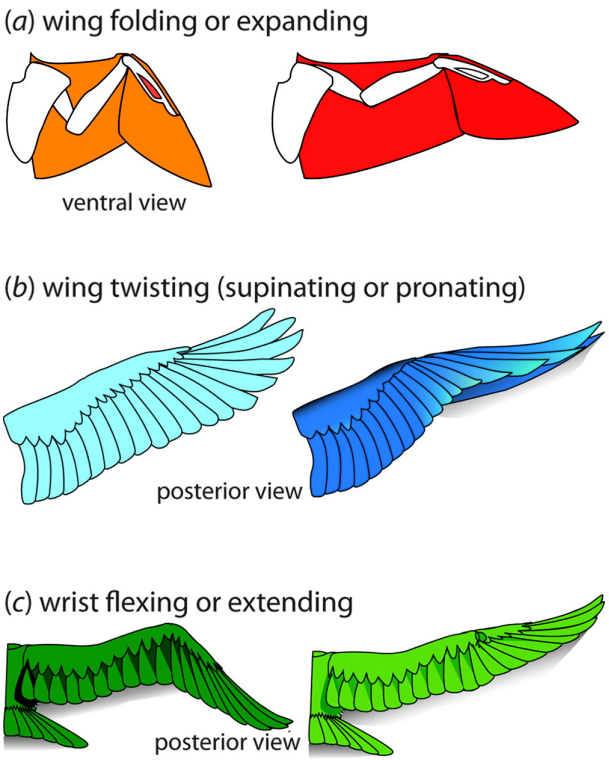

Figure 2.3: Exemple of the functional movement of the wing [4].

The shoulder will be modelled by 3 revolute joints (equivalent to a spherical joint), the elbow and the wrist will both be modelled with 2 revolute joints:

- The folding and expanding of the wing requires revolute joints along the dorso-ventral axis (blue cylinder in Figure 2.4, R3 joint in Robotran) of the bird at each articulation, as shown in Figure 2.3 (a).

- The supination and pronation of the forearm is a twisting motion along it. This torsion is uniform along the forearm, as illustrated in Figure 2.3 (b). But this must be adapted to suit the rigid multi-body system formalism. This is why we have a revolute elbow joint along the transverse axis, i.e. aligned with the forearm (green cylinder in Figure 2.4, R2 joint in Robotran). This degree of freedom is essentially used to adjust the angle of attack for the distal part of the wing.

- The flexing and extending of the wing requires a revolute joint along the longitudinal axis (red cylinder in Figure 2.4, R1 joint in Robotran) of the bird at the wrist, as presented in Figure 2.3 (c).

- The shoulder must orient the whole wing compared to the body. It requires a revolute joint along the transverse axis (R2 joint in Robotran). The shoulder must also perform the flapping motion of the entire wing relative to the body. It requires a revolute joint along the longitudinal axis (R1 joint in Robotran) of the bird at the wrist.

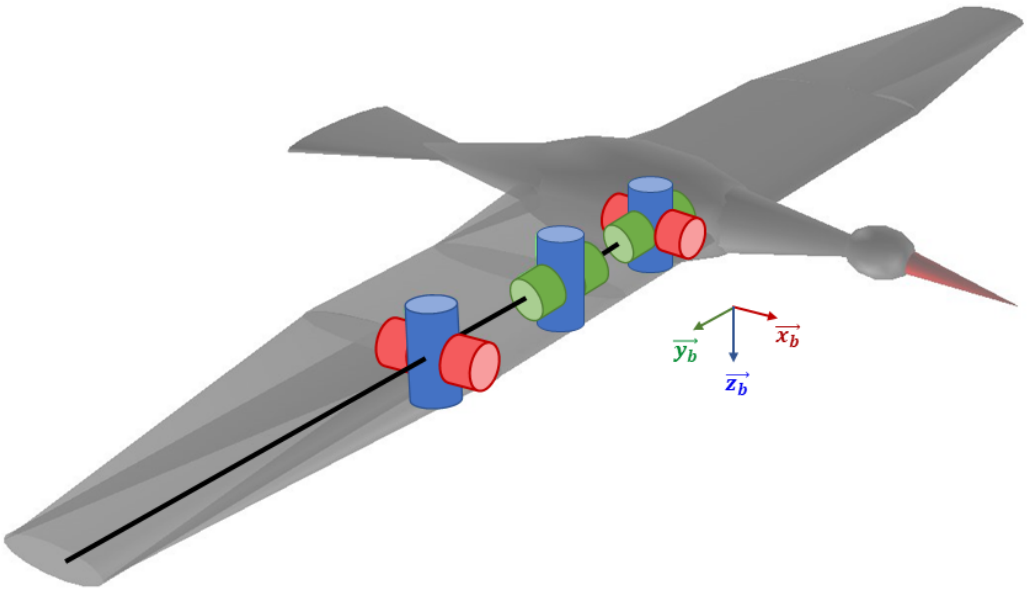

Figure 2.4: Representation of the right wing revolution joints.

2.1.2 Multi-body system with articulated wings

The bird body is modeled as a 3D multi-body system formed by rigid bodies. It consists of 7 anatomical segments: torso (main body), two arms, two forearms and two hands. The global axes are $\hat{X}_e$ and $\hat{X}_b$. The multi-body system is made of 20 joints. Each wing is articulated with 7 revolute joints, as mentioned before. The main body of the bird have 6 joints (3 prismatic joints and 3 revolute joints along the body frame). The 3 revolute joints of the main body are link to the roll, pitch, yaw angle of the bird.
The set of 20 independent coordinates (as many as the system DOFs) formed by the Cartesian coordinates of the position vector of the gravity center of the main body (q_1, q_2, q_3 in Figure 2.5) and the 17 angular coordinates that define the relative orientation of each body compared to its "parent" body ($q_4, ..., q_{20}$ in Figure 2.5).

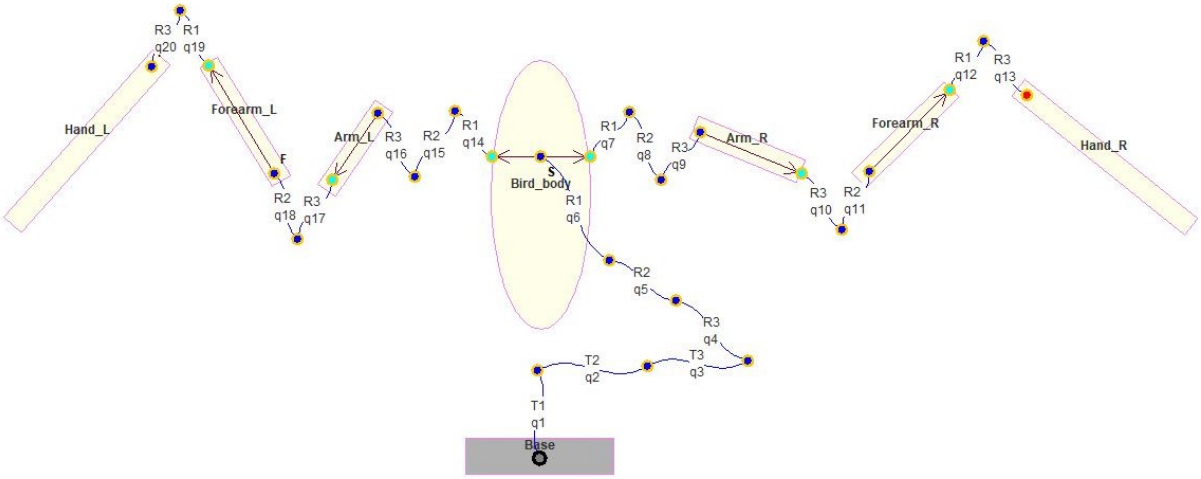

Figure 2.5: Representation of the multi-body system in MBsysPad.

The wing sections are defined by their chord length distribution and a cross-section, which is scaled with the chord. The chord length distribution is obtained thanks to 7 lengths (c_1, c_2, c_3, c_4, l_A, l_F, l_H) indicated in Figure 2.7. The root chord and the tip chord are respectively noted c_1 and c_4. c_2 and c_3 are the proximal and distal intermediate chords. l_A, l_F and l_H are respectively the transverse length of the arm, forearm and hand sections. Their numerical values are given in Appendix A. Furthermore, we assume that the line passing through 1/4 of the chord length is a straight line, which corresponds to the lifting line of the wing section. Thus, the leading and trailing edges are tapered (trapezoidal).

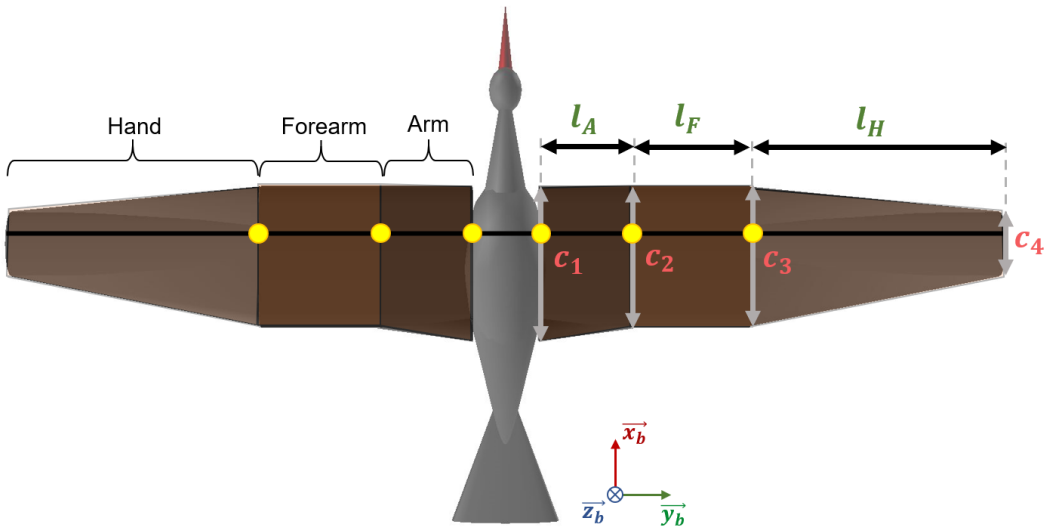

Figure 2.6: Sections of bird wings and joints (yellow dots)

In order to calculate the dynamics of the multi-body, it is essential to know the mass and inertia of each body. The body mass is obtained by the homogeneous density of the bird's body multiplied by the volume of the body. The numerical values and details are in Appendix A. The masses of the wing sections are obtained by the homogeneous density of the bird's wing multiplied by the volume of the wing sections. So we need the volumes of the bodies. For the wing sections, we have created a cross-section that adjusts according to the chord length (Figure 2.7). We developed it so that the geometric center of the surface is at 1/4 of the chord length. This means that the center of gravity of a segment lies on the lifting line of the segment. It is important to specify that this cross-section is not the aerodynamic profile used to calculate the aerodynamic forces.

$$\frac{z(\frac{x}{c})}{c} = \begin{cases} \pm\frac{\sqrt{1-(\frac{4x}{c})^2}}{d_1} & \frac{x}{c} \in [0, \frac{1}{4}] \\ \pm d_1\left(1 + \frac{(1-\gamma)}{d_2}\frac{x}{c}\right) & \frac{x}{c} \in [\frac{-1}{12}, 0] \\ \pm d_1\gamma\left(1 + \frac{\frac{x}{c}+d2}{\frac{3}{4}-d_2}\right) & \frac{x}{c} \in [\frac{-3}{4}, \frac{-1}{12}] \end{cases}$$

Condition that ensures that the geometric center of the surface lies at 1/4 of the chord length:

$$d_2 = \frac{3\gamma}{2}\left(1 - \sqrt{1 - \frac{4}{\gamma}\left(1 - \frac{2}{9\gamma}\right)}\right)$$

$d_1 \equiv$ The half thickness at $\frac{x}{c} = 0$
$\gamma \equiv$ The half thickness ratio for $\frac{z}{c}$ at d_2 and 0
$d_2 \equiv$ Transition in x axis to the feather-like part of the cross-section

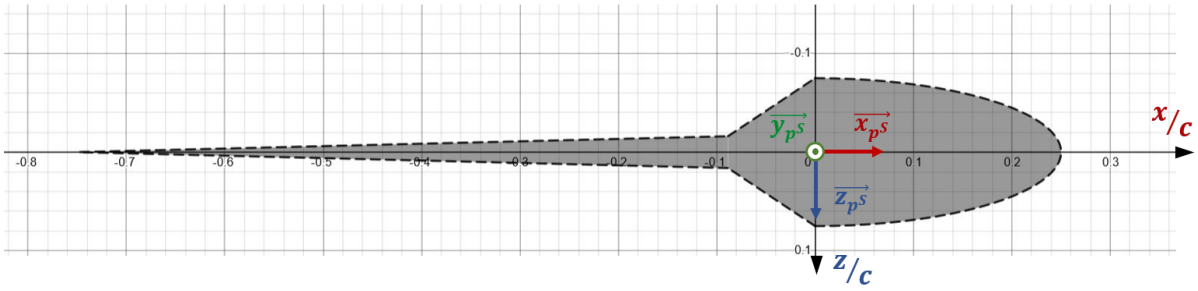

Figure 2.7: Cross-section of the wing section with $d_1 = 0.075$, $d_2 = 1/12$ and $\gamma = 0.215$

The main body is approximated by an ellipsoid (Figure 2.8), which has the same length on two axes (i.e. an ellipsoid of revolution also called a spheroid). The third axis is the longitudinal axis and it is longer than the other two (i.e. an prolate spheroid).

$$\text{Main body} \approx \text{prolate spheroid} \triangleq \frac{x^2}{(l_B/2)^2} + \frac{y^2 + z^2}{(l_{ICS}/2)^2} = 1$$

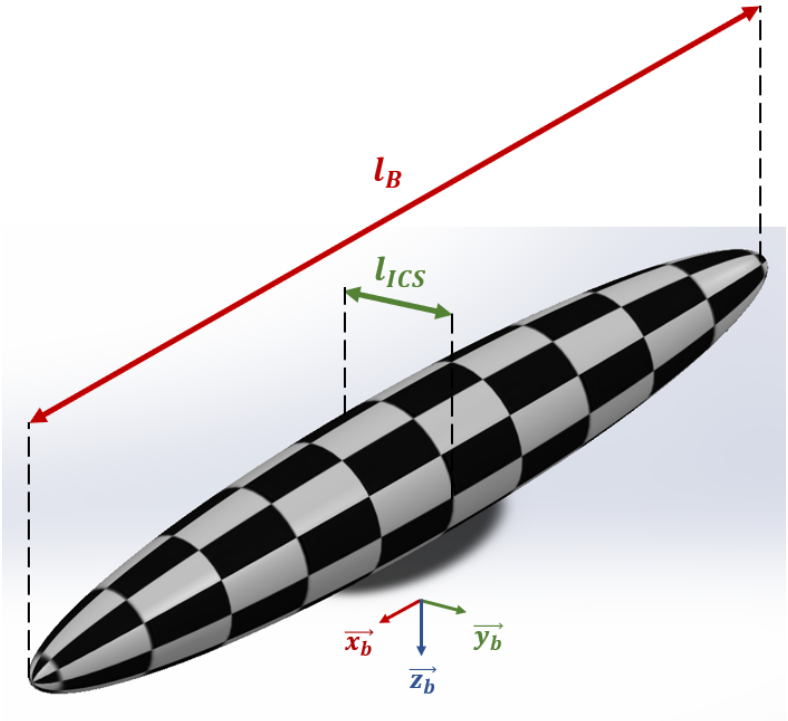

Figure 2.8: The main body representation

2.2 Musculoskeletal model

In this chapter, we will describe and represent the interconnection between the skeleton and the muscles. Muscles are used to perform skeletal movements such as flight locomotion and maintenance of posture. The anchoring to the bone is done by the tendons.

This work focus on forelimbs. 10 muscles have been considered in each wing of the model. According to the aims of the studies the number of muscles can be reduced. For example, to estimate the muscular forces during level flapping flight, muscles on the right wing have only been considered due to the symmetric behaviour, whereas to estimate the whole energy consumption only these muscles have been take into account.

A constraint for each muscle is necessary for loop closure in the multi-body tree (Kinematics loop). These are the only Kinematics loop, because we do not consider the ground (and ground contact).

A musculo-skeletal system was developed to drive the 7 forelimb DOFs. The model actuates each wings with 10 muscles, capturing the contribution of the main muscle of the bird forelimbs. For our IbisCUS model, these virtual muscles produce torque. The key idea is that muscles react by contracting and apply forces on the body. Therefore, the equivalent torques applied by the 10 muscles on the wing joints are computed from the segments free-body diagrams. The muscle state computation is fully described in Chapiter 4. The main muscle properties are scaled to fit the size and the weight of the Northern Bald Ibis, using scaling detail in Chapiter 5. Each muscle is then controlled by its activation $a_m(t)$, capturing the neural signal provided by motor neurons. This signal is related to a neural input $s_m(t)$, the muscle stimulation. Controlling the muscle model thus reduces to designing control rules for the stimulations $s_m(t)$ driving the 10 muscles of the wing.

2.2.1 Musculoskeletal geometry

The musculotendon length (l_{mtu}), musculotendon velocity (v_{mtu}), and moment arms of a muscle depend directly on the musculoskeletal geometry as well as on body segment configurations. These variables play an important role in generating joint torques.

Origins and insertions

Although many muscles associated with flight have multiple origins and/or insertions, for this analysis, we modeled all muscles with a single point of origin and a single point of insertion. These points correspond to the attachment of muscle tendon unit (MTU) to bones and are defined as muscle origin (i.e. proximal attachment) and muscle insertion (i.e. distal attachment). The locations of the origin and insertion of the muscle are noted respectively $\vec{r}_{ori}$ and $\vec{r}_{ins}$ in the distal bones (i.e. distal attachment segment) local frame.

The muscle origin vector is a constant in the proximal bone (i.e. proximal attachment segment) local frame $\vec{R}_{ori}$. That is why it is stored in this form in MBsysPad (cfr Robotran). In Figure 6, the example of a mono-articulated muscle is represented with the main vector quantity.

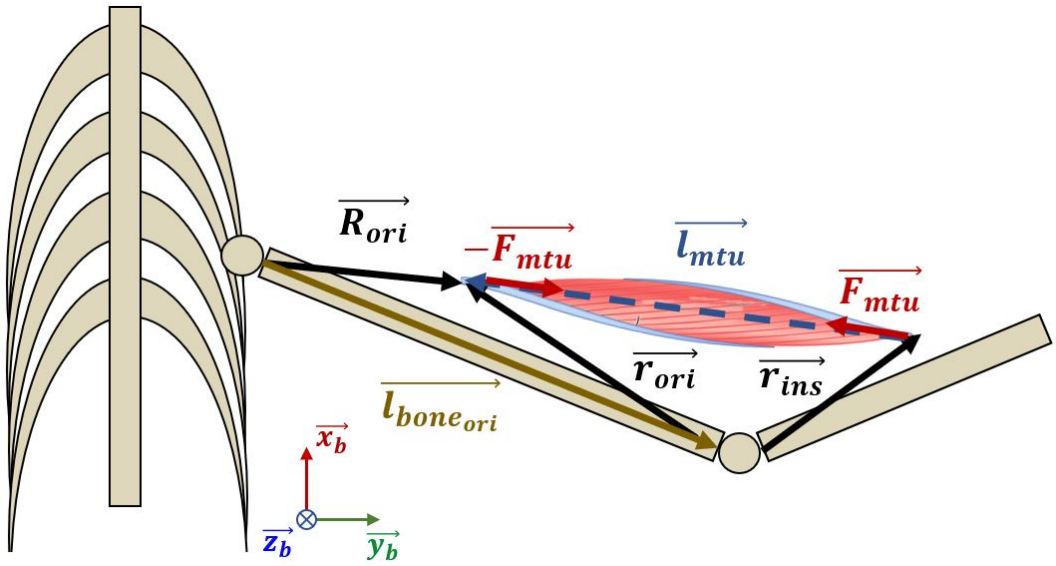

Figure 2.9: Exemple of the musculoskeletal geometry of a muscle.

For a mono-articulated muscle, $\vec{r}_{ori}$ is obtained as follows:

$$\vec{r}_{ori} = \underline{\underline{R}}^{ins}_{ori}(\vec{R}_{ori} - \vec{l}_{bone_{ori}})$$

$\underline{\underline{R}}^{ins}_{ori}$ is the rotation matrix between the origin and insertion frame.

The musculotendon force vector ($\vec{F}_{mtu}$) can be expressed as the unit vector $\vec{u}_{mtu}$. Which is the direction along the line of action of the muscle multiplied by the force magnitude $||\vec{F}_{mtu}||$:

$$\vec{F}_{mtu} = ||\vec{F}_{mtu}|| \cdot \vec{u}_{mtu}$$

The unit vector of the muscle line of action for a mono-articulated muscle is given by:

$$\vec{u}_{mtu} = \frac{\vec{r}_{ori} - \vec{r}_{ins}}{||\vec{r}_{ori} - \vec{r}_{ins}||} = \frac{\vec{l}_{mtu}}{||\vec{l}_{mtu}||}$$

The origins and insertions points of the muscles have been taken from [5].

Muscles moment arms

The musculotendon force is not the final goal since it is the torque generated by these muscles at the joints, which will actuate the skeleton in addition to the external forces.

$$\vec{\mathcal{T}}_{mtu} = \vec{r}_{ins} \times \vec{F}_{mtu} = ||\vec{F}_{mtu}|| \cdot \underbrace{\vec{r}_{ins} \times \vec{u}_{mtu}}_{\triangleq \vec{r}_{mtu}} = F_{mtu} \cdot \vec{r}_{mtu}$$

$$\vec{r}_{mtu} = \vec{r}_{ins} \times \vec{u}_{mtu} = \vec{r}_{ins} \times \frac{\vec{r}_{ori} - \vec{r}_{ins}}{||\vec{r}_{ori} - \vec{r}_{ins}||} = \frac{\vec{r}_{ins} \times \vec{r}_{ori}}{||\vec{l}_{mtu}||}$$

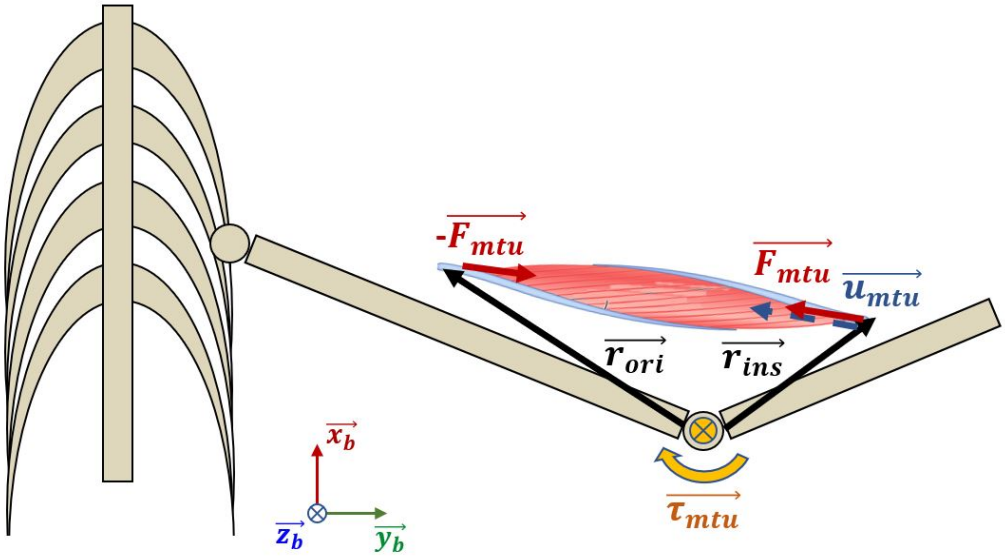

Figure 2.10: Exemple of the musculoskeletal geometry of a muscle. The vector u_{mtu} is the muscle force unit vector.

With $\vec{r}_{mtu}$ for all the muscles at each joint they influence, we can build the Jacobian of the muscular lever arms ($\underline{\underline{J^T}}$),which is a function of the skeletal state ($\underline{q}$). Such that for m muscles and n joints, $\underline{\underline{J^T}}$ will be of dimension nxm and will provide the torques due to the muscles ($\underline{\mathcal{T}_m}_{nx1}$) as a function of the magnitude of the muscle forces ($\underline{F_m}_{mx1}$):

$$\underbrace{\begin{bmatrix}\mathcal{T}_1 & . & . & . & \mathcal{T}_n\end{bmatrix}^T}_{\underline{\mathcal{T}_m}_{nx1}} = \underline{\underline{J^T}}(\underline{q})_{nxm} \underbrace{\begin{bmatrix}F_1 & . & . & . & F_m\end{bmatrix}^T}_{\underline{F_m}_{mx1}}$$

In most biological systems, there are more muscles than degrees of freedom to be driven. This is also our case n=7 and m=10, therefore $\underline{\underline{J^T}}$ is not a square matrix. For the inverse dynamics the inversion of $\underline{\underline{J^T}}$ will require to solve the overacting problem.

Figure 2.11 shows the addition and implementation of the geometry of the muscles in connection with the bone. This is an update of Figure 2.5. All that is related to the muscles themselves and the selection of them is explained in Chapter 4.

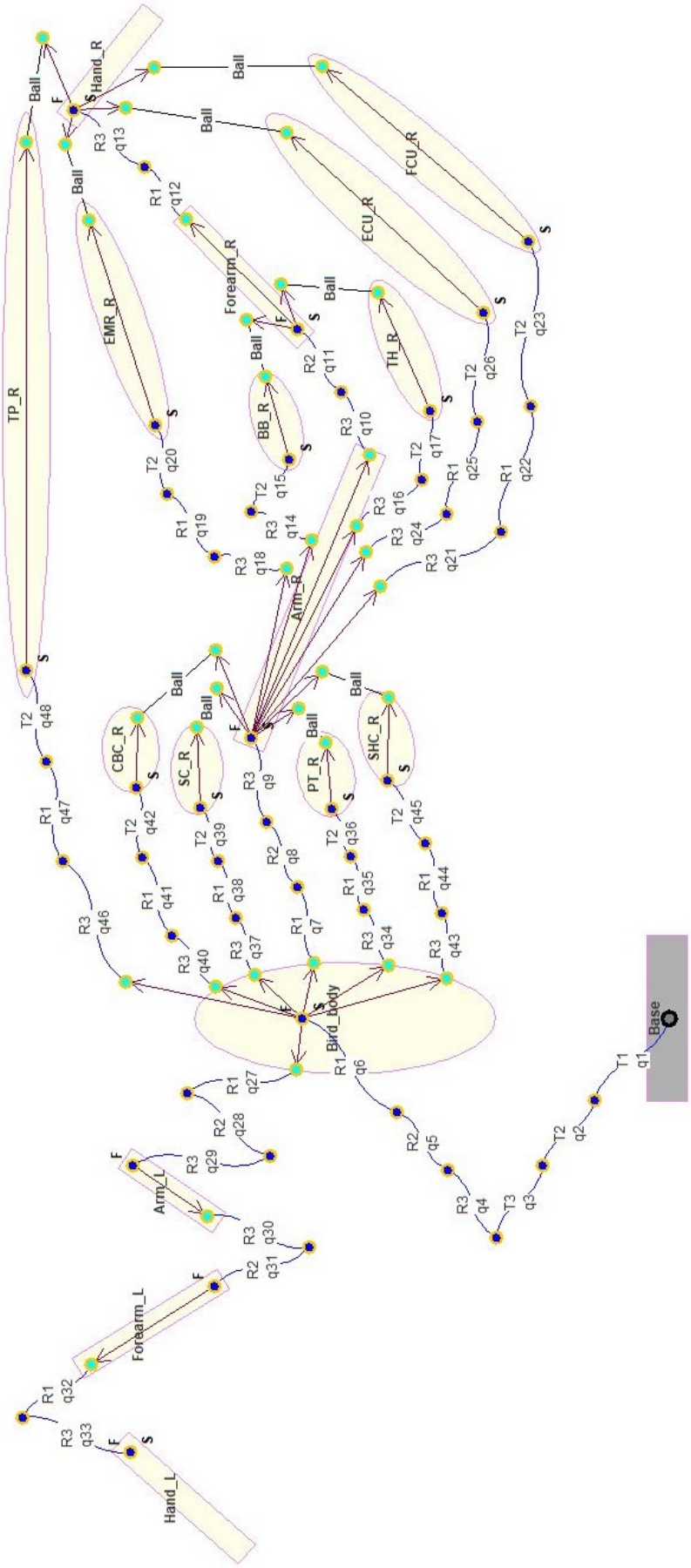

Figure 2.11: Representation of the multi-body system with the muscles in MBsysPad.

CHAPTER 3

Aerodynamic model

This thesis features a biomechanical model based on the anatomy of a bird, that models the wing section of the wing. For this we need the external forces that apply to the multi-body system. These are the aerodynamic forces in our case. The aerodynamic solver relies on a thin airfoil theory method (we do not consider the wake). The code was provided by Victor Colognesi and then adapted. We will not spend too much time on the aerodynamics model. Because there are codes within the ReavelFlight project that are much more detailed, like the one made by Victor Colognesi. Which can calculate the wake and model the feathers [2].

Before entering into the heart of the subject, we will define the main reference frame that will be used in this work. We adapt to the bird the conventional axes of fixed-wing aircraft flight dynamics:

The wind frame is a practical frame for expressing the aerodynamic forces and moments acting on a bird. Indeed, the net aerodynamic force can be divided into its components along the wind frame axes, with the drag force in the $-\vec{x_w}$ direction and the lift force in the $-\vec{z_w}$ direction.

Wind frame $\hat{X_w}$:

- $\vec{x_w}$ axis: positive in the direction of the velocity vector of the bird relative to the air ($\vec{V_{rel}}$).
- $\vec{z_w}$ axis: perpendicular to the $\vec{x_w}$ axis, in the plane of symmetry of the bird, positive below the bird.
- $\vec{y_w}$ axis: perpendicular to the $\vec{x_w}$,$\vec{z_w}$-plane, positive out the right wing (i.e. determined by the right-hand rule).

The various angles relating the reference frames are explained below. We use the convention of Tait-Bryan angles. It means that the rotation sequences used is z-y'-x". Based on the rotations and axes conventions above:

- Tait-Bryan angles from Earth frame to wind frame:
  - Heading angle σ: angle between north and the projection of $\vec{x_w}$ onto the horizontal plane. It describes in which direction the bird is moving relative to cardinal directions (i.e. the "cap" in french).

  - Flight path angle γ: is the angle between horizontal plane and the velocity vector, which describes whether the aircraft is climbing or descending.
  - Bank angle μ: rotation of the lift force around the velocity vector, which may indicate whether the airplane is turning.

  Flight path angle and bank angle form the attitude of the bird.

- Tait-Bryan angles from wind frame to body frame:
  - Sideslip angle β: angle between the velocity vector and the projection of $\vec{x_b}$ axis onto the $\vec{x_w}$,$\vec{y_w}$-plane, which describes whether there is a lateral component to the aircraft velocity.
  - Angle of attack (AoA) α: angle between the $\vec{x_w}$,$\vec{y_w}$-plane and $\vec{x_b}$ axis. $\alpha = \Theta - \gamma$.
  - Nothing for the equivalent of the roll here because it does not change anything.
- Tait-Bryan angles from wind frame to wing section p and side S frame:
  - Wing Sideslip angle β_p^S: angle between the velocity vector and the projection of $\vec{x_p^S}$ axis onto the $\vec{x_w}$,$\vec{y_w}$-plane, which describes whether there is a lateral component to the wing section velocity.
  - Wing Angle of attack α_p^S: angle between the $\vec{x_w}$,$\vec{y_w}$-plane and $\vec{x_p^S}$ axis of the wing section. Pay attention, it is this AoA that is important to determine the magnitude of the aerodynamics forces on the wing section p .
  - Nothing for the equivalent of the roll here because it does not change anything.

These sets of angles are analogous:

- x axis: Yaw/ Heading angle/ Sideslip angle/ Wing Sideslip angle
- x axis: Pitch angle/ Flight path angle/ Angle of attack/ Wing angle of attack
- x axis: Roll angle/ Bank angle

The objective of straight and level flight results in a zero time average of the flight path angle over a flight period T_{flight}(i.e. time of a flapping flight cycle).

$$\text{Straight and level flight} \equiv \frac{\int_{t_0}^{t_0+T_{flight}} \gamma(t)dt}{T_{flight}} = 0$$

3.1 Aerodynamic forces formulation

3.1.1 Wing sections aerodynamic forces

The wing kinematics are imposed based on biological observations in chapter 5. In this work, we calculate the aerodynamic forces experienced by the flyer, through the integral of the lift and drag components along the discretised wing. Thanks to the thin airfoil theory, we know that the aerodynamic center is exactly one quarter of the chord behind the leading edge. This theory idealizes the flow along an airfoil as a two-dimensional flow around a thin airfoil which can be considered as tending towards a zero thickness airfoil. The profiles for C_l and C_d versus the angle of attack of the airfoil have been provided.

3.1.2 Bird's body drag force

To go a step further and take into account the body of the bird from an aerodynamic point of view, we consider the drag of it. For that we express the

This additional force is applied to the center of gravity of the bird's body and is aligned with the instantaneous relative air velocity with respect to the bird's body (i.e. $-\vec{V}_{rel}$):

$$\vec{D}_{body} = -D_{body} \cdot \frac{\vec{V}_{rel}}{||\vec{V}_{rel}||} = -D_{body}\, \vec{x}_w$$

Its magnitude (D_{body}) is calculated as follows:

$$D_{body} = \frac{1}{2} C_{d,body} \cdot \rho_{air} \cdot S_b \cdot ||\vec{V}_{rel}||^2$$

where $C_{d,body}$ is the drag coefficient of the body, ρ_{air} the air density and S_b the frontal surface of the body. The method proposed in [6] is applied to evaluate the values of the frontal area (Equation 3.1) and the drag coefficient (Equations 3.2 and 3.3):

$$S_b \approx m_{bird}^{\frac{2}{3}} \cdot 8.13 \times 10^{-3} = 9.179 \times 10^{-3} m^2 \tag{3.1}$$

$$C_{d,body}(Re) \approx \begin{cases} 0.25 & Re \geqslant 2 \times 10^5 \\ 1.57 - 0.108 \ln(Re) & Re \in [0.5 \times 10^5, 2 \times 10^5] \quad \text{transitional region} \\ 0.4 & Re \leqslant 0.5 \times 10^5 \end{cases} \tag{3.2}$$

$$Re_{body} \approx Re_{body}(\text{at max range speed}) \approx \sqrt{m_{bird}} \cdot 1.25 \times 10^5 = 1.37 \times 10^5 \tag{3.3}$$

By inserting the result of equation (3.3) into equation (3.2), the estimate of $C_{d,body}$ is obtained and is equal to 0.2926. The equivalent flat plate of the body area (A_b) is obtained by the product of S_b and $C_{d,body}$:

$$A_b = S_b \cdot C_{d,body} = 2.686 \times 10^{-3} m^2$$

The expression of D_{body} becomes:

$$D_{body} = \frac{A_b \cdot \rho}{2} ||\vec{V}_{rel}||^2$$

In Figure 3.1, The Northern Bald Ibis is represented by three circles of area S_w, S_b and A_b.
For example,as said in [6], the ratio between S_w and A_b can be used to estimate its maximum effective lift to drag ratio in the case of "ideal bird":

$$\left(\frac{L}{D}\right)_{max} = \sqrt{\frac{S_w}{A_b}} = 23.09$$

Nevertheless, the actual value will be rather around half of the ideal value, which is in line with [7] and [8].

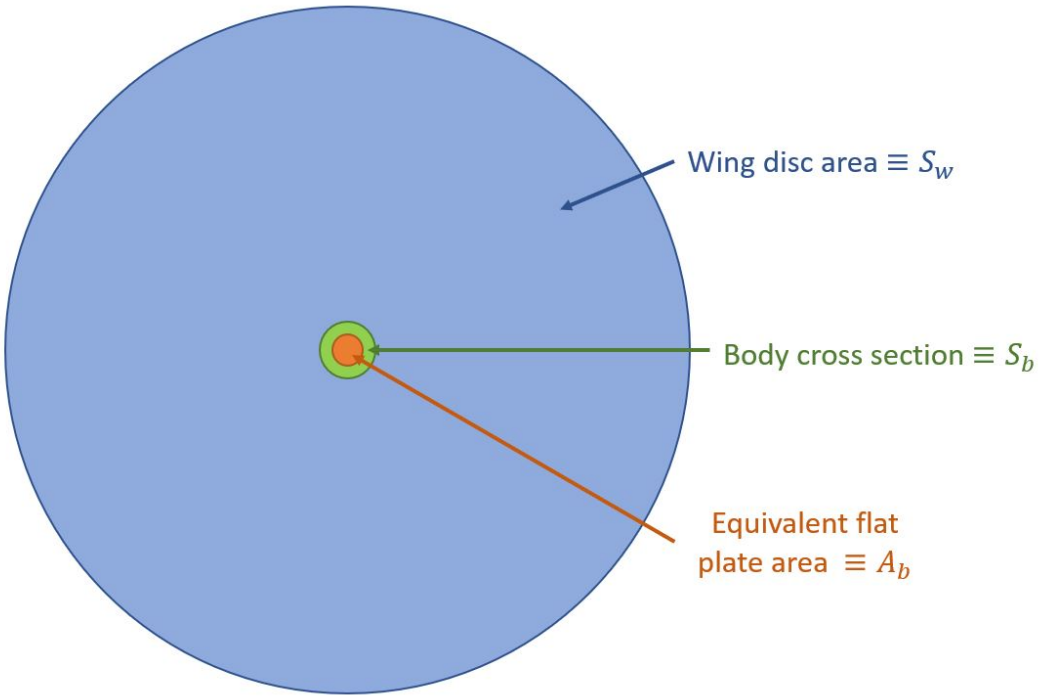

Figure 3.1: The large blue circle is the wing disc, whose area is S_w, and whose diameter is equal to the wing span WS. The green inner circle is the body cross-section at the widest part, whose area is S_b the body frontal area. The small orange circle is the equivalent flat plate, whose area A_b is one third of S_b. Diagram draw on scale. Inspired form Fig.3.6 in [6]

CHAPTER 4

Muscle model

The aim of this chapter is to study and model the muscle tendon unit (MTU). The internal forces generated by the muscles need to be known in order to move the skeleton. This is achieved with a bio-inspired approach, meaning that the muscle forces are generated by neural stimulation and depend on the state of the body (more precisely the state of muscle tendon unit). In addition, they are limited by a series of physical and biological constraints.

4.1 Introduction

The muscle actuator modeling has three basic pillars: one is the musculoskeletal geometry, the second is the muscle activation dynamics and the third is musculotendon dynamics. These three basic pillars interact with each other. The first one defines the environment in which the muscle evolves. The second one represents the behavior of the motor nerves that transmit the motor commands from the central nervous system (CNS) to the muscles, which will activate the contraction of the muscle fibers. The third one represents the response of the muscle tendon unit to the muscle activation, taking into account the state of its anchoring points on the bones. In this study, the tendon muscle unit will be described thanks to a Hill-type muscle model. According to this model, the dynamics of musculotendon actuators can be divided into the activation dynamics and the musculotendon contraction dynamics (as explained in [9]). They are assumed to be cascaded and decoupled processes.

The geometry of the musculoskeletal system has already been covered in the previous chapter. First, we will start with the musculotendon contraction dynamics, which refers to the conversion of the activation into a muscle force. The muscle and tendon properties, such like the tendon compliance (i.e. reciprocal of stiffness) will be described as well. It links the deformation of tendon and the tendon stress. Then, we will continue with the selection of muscles used for the model approximation. Afterwards, we need numerical data specific to our bird of interest to run the simulation. We will cover the evaluation of the specific parameters and their adjustment. The muscles will have the freedom to be tilted (pennated) in regards to the tendons, as they could be in real living organisms. The pennation will be considered and its influence on the muscular behavior will be examined. Next, we will look at the comparison between the activation dynamics and the musculotendon contraction dynamics in terms of their characteristic time. Thus, we

will cover the activation dynamics, which refers to the conversion of a neural excitation (stimulation) into an activation of the contractile fibers. We will end this chapter by explaining the simulation scheme of the muscle model.

As illustrated in Figure 4.1, the whole diagram for modeling the muscle is represented with all of its components.

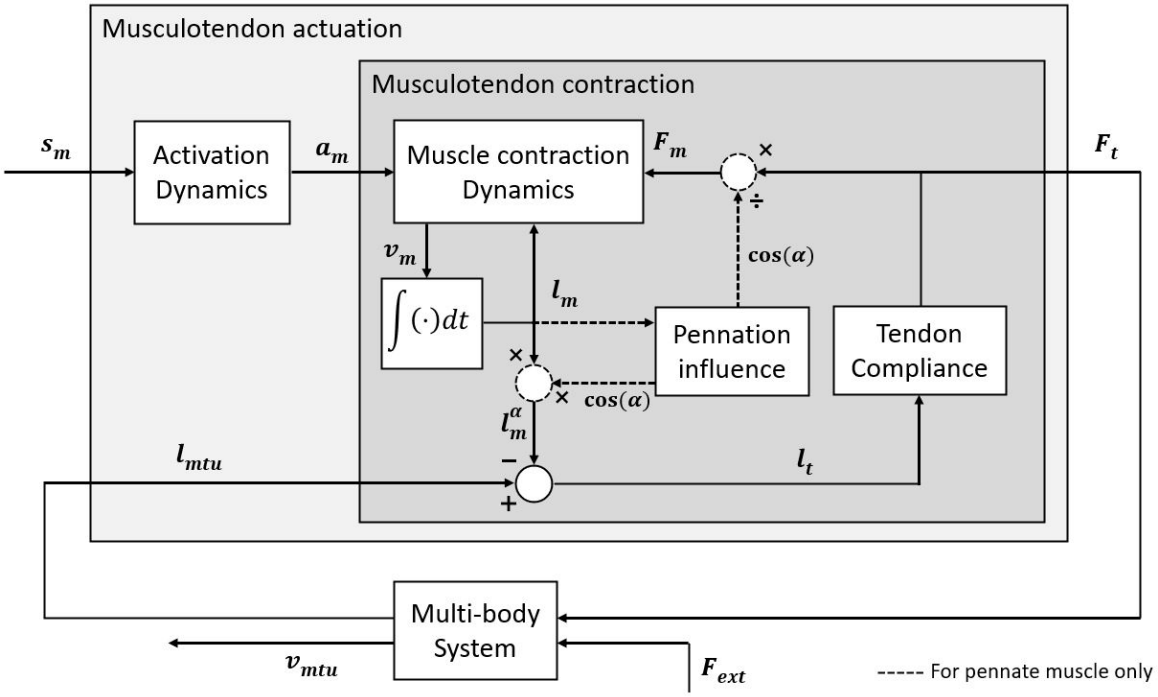

Figure 4.1: Architecture of the muscle module code. The neural controller generates the neural stimulation (s_m) that excites the musculotendon unit by a muscular activation (a_m). The muscle tendon unit produces a force (F_t) depending on a_m and the musculotendon length (l_{mtu}). F_t actuates the skeleton thanks to the resulting joint torques.

4.2 Musculotendon contraction dynamics

Muscles are constituted with bundles of fibers and tissues. The anchorage to the bone is achieved by the tendons. The fibers can be oriented at an acute angle (i.e the pennation angle α) with respect to the tendon as shown in Figure 4.2. This kind of muscle is called a pennate muscle. If the fibers are oriented parallel to the tendon. The muscle is called a parallel muscle.

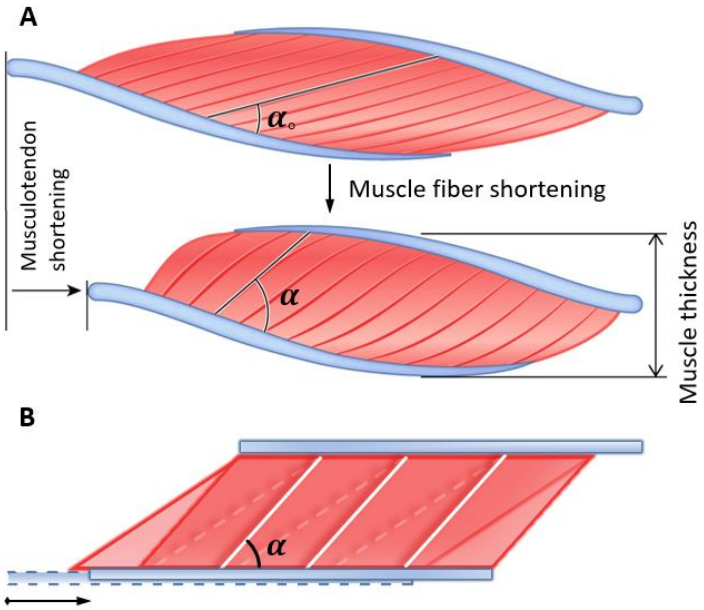

Figure 4.2: Pennate muscle representation with the muscle (light red) and tendon (light blue).
A: The upper snapshot shows a relaxed pennate muscle and the lower snapshot shows the same muscle when it is contracted. This highlights the fibers rotation, the angle of pennation increases with the tension. The shortening of the muscle fibers is associated with a greater musculotendon shortening, which is due to the effects of fiber pennation. Adapted form Fig.1 in [10]
B: Simplified representation of the muscle with the assumption that its thickness remains constant. Inspired form Fig.2 in [11]

The muscle tendon unit model can be seen as a passive structure and a physiological actuator,which will generate forces. The Hill-type muscle used is described in section 4.2.1. The dimensionless mechanical model used is described in section 4.2.3. These dimensionless equations are the result of the dimensional analysis of the equations performed in section 4.2.2.

4.2.1 Muscle tendon unit representation

A Hill-type muscle model is used to evaluate the force developed, produced by the musculotendon actuator. A comparison between different muscular models was done in [12]. Our choice is motivated by the features of this model mentioned in this article: *"The main advantages of this model are its simplicity and its direct connection with the macroscopic*

muscle experiments. [...] It has been developed more than hundred years ago and is now widely used. This model is almost universally accepted as an appropriate phenomenological and mathematical representation of the muscle dynamics. [...] The Hill model is, as was already mentioned, a phenomenological model based on interpretations of input and output data obtained during experiments." Furthermore, unlike other models, it does not requires the microscopic data such as the chemical data of muscle.

In short, this model requires few muscle dependent parameters, has fast computation time, allows the implementation of pennation, is suited for multi-body simulations with many muscles and still has physical meaning from a phenomenological point of view. These are the reasons that make the Hill-type muscle model the most appropriate model with respect to the available information and the objective of this work, which is to find the force response of the muscle.

Two types of elements can be distinguished (Figure 4.3): passive and active elements. The only active element in the hill muscle representation is the contractile (CE) one. It means that, the CE element depends on an additional input. The input is the muscle activation is described in more detail in Section 4.7.

The mechanical model used to represent the muscle tendon unit is made up of a passive serial elastic element (SE), an active contractile element (CE), a passive parallel elastic element (PE), and a passive buffer elastic element (BE) as illustrated in Figure 4.3.

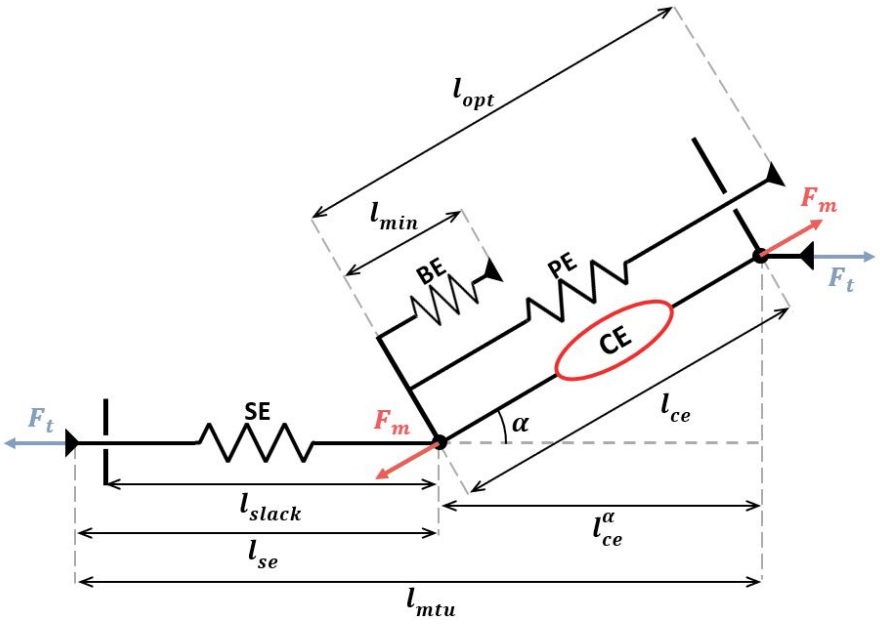

Figure 4.3: Mechanical modelling of Hill-type muscle with serial (SE), contractile (CE), parallel (PE) and buffer (BE) elements with pennation angle α.

For this muscle modelisation, the pennation angle is taken into account in the representation of the virtual muscle as shown in Figure 4.5. The pennation angle aspects are described in more detail in Section 4.5. The arrangement of the muscle tendon unit can be seen in Figure 4.4.

For a pennate muscle, the relationship between the musculotendon length l_{mtu}, the muscle fiber length l_m, the tendon length l_t, and the pennation angle is given by:

$$l_{mtu} = l_t + l_m \cdot \cos(\alpha)$$

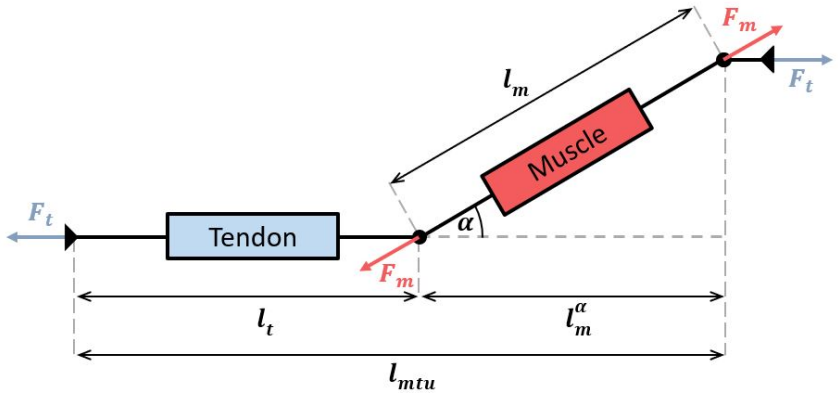

Figure 4.4: Muscle (light red) and tendon (light blue) configuration representation with pennated muscle fibers (of an angle α).

Since the the muscle element and the tendon element are in series, the forces through both elements must be the same. The relationship between the musculotendon force F_t, the muscle force F_m and the pennation angle is given by:

$$F_t = F_m \cdot \cos(\alpha)$$

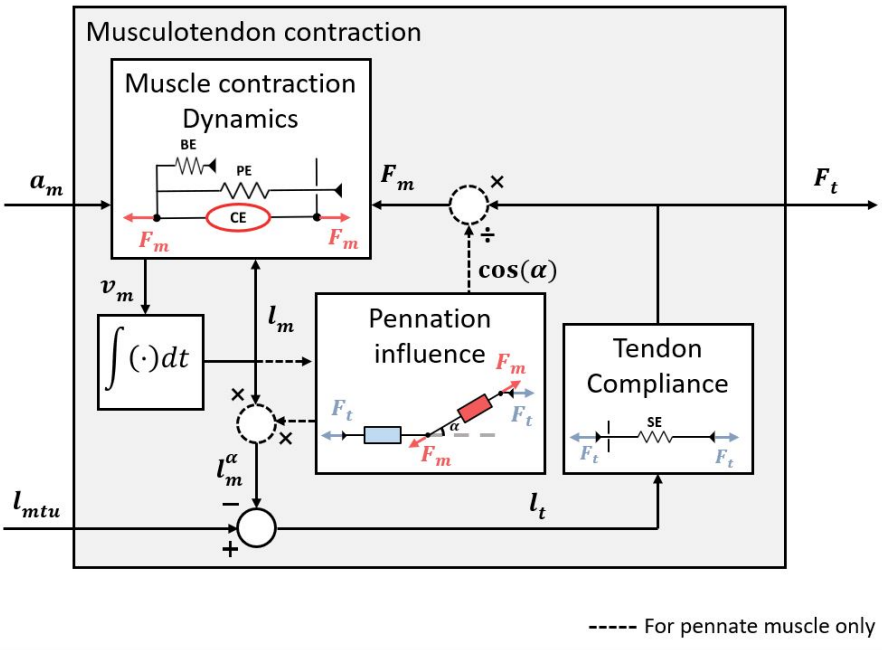

Figure 4.5: Diagram of the musculotendon contraction dynamic. Based on the muscular activation (a_m), the musculotendon length (l_{mtu}), the muscle tendon unit produces force (F_t) and actuates the skeleton thanks to the resulting joint torques.

The force of the muscle tendon unit is the projection of the muscle force onto the line of action of the muscle tendon unit. For the same muscle strength, a larger pennation angle will decrease the strength of the muscle tendon unit. However, the pennate muscle has more fibers that get through the cross-section area (i.e. the muscle characteristics like the physiological cross-section area of the muscle PCSA and the maximum isometric stress F_m^{iso} are higher for pennate muscle).

4.2.2 Muscle dimensional analysis

The dimensional analysis is performed using Buckingham's Π theorem to obtain dimensionless Π groups.

> ◇ ***The Buckingham's Π theorem*** *states that:*
> *If there are n variables (v_1, v_2 ,..., v_n) in a problem and these variables contain r primary dimensions (e.g. M, L, T): $v_1 = f(v_2, v_3, ..., v_n)$*
> *The equation relating all the variables will have (n-r) dimensionless groups (i.e. Π groups).*
> *The final equation obtained is in the form of : $\Pi_1 = \phi(\Pi_2, \Pi_3, ..., \Pi_{n-r})$*
> *The Π groups must be independent of each other.*

This method offers the advantage of solving dimensionless equations that can describe the behaviour of a set of different systems that share the same values of these dimensionless numbers (Π groups). However, the choice of dimensionless parameters is not unique.

The Hill's model has four muscle-specific parameters and one tendon-specific parameter:

- The maximum isometric force of the muscle F_m^{iso}
- The optimal length of the muscle l_{opt}
- The maximum shortening velocity of the muscle at null load v_{max} (defined as negative)
- The muscle thickness w_t is required in the case of pennate muscle.
- The length for which the tendon begins to produce force l_{slack} (i.e. the length at which the tendon is slacked)

Thanks to the Buckingham's Π Theorem, we know that we will have 3 dimensional variables and 2 dimensionless variables. Then a dimensionless model generic among all muscles can be formulated with 2 dimensionless parameters. The dimensionless muscle model is scaled thanks to 3 physical parameters F_{iso}^m, l_{opt} and the muscle time-scaling parameter $t_s = -\widetilde{v_{max}}^{-1} = \frac{l_{opt}}{-v_{max}}[s]$ (with $\widetilde{v_{max}}$ the normalised maximum shortening velocity). The 2 dimensionless parameters are $\widetilde{l_{slack}} \triangleq \frac{l_{slack}}{l_{opt}}$(i.e the dimensionless slack length of the tendon) and $\widetilde{w_t} \triangleq \frac{w_t}{l_{opt}} = \sin(\alpha_0)$. In the following, we will use the optimal pennation angle α_0 instead of the normalised muscle thickness $\widetilde{w_t}$ for convenience. The optimal pennation angle of the muscle fiber α_0 is the pennation angle of the muscle fibers at the optimal length of the muscle.

Hence, these 2 dimensionless parameters (α_0 and $\widetilde{l_{slack}}$) are the parameters of the generic dimensionless model. In the case of parallel muscle, the dimensionless model has only one remaining parameter ($\widetilde{l_{slack}}$).

The Hill's musculotendon model specific parameters are F_m^{iso}, l_{opt}, t_s (or $\widetilde{v_{max}}$), $\widetilde{l_{slack}}$ and α_0.

Here is 3 compact notations:

- The $\widetilde{l_x} \triangleq \frac{l_x}{l_{opt}}$ denotes the dimensionless length of x normalised with l_{opt}.
- The lowercase $f_x \triangleq \frac{F_x}{F_m^{iso}}$ stands for the dimensionless force of x normalised with F_m^{iso}.
- The $\mathring{\phi} \triangleq \dot{\phi} \cdot t_s$ signifies the dimensionless time derivative of ϕ in terms of the dimensionless time $\tau = t/t_s$

4.2.3 The dimensionless musculotendon formulation

The relationships of this model are based on experimental data. Hence, they present a phenomenological meaning. The equations presented in this section were defined in the article of Geyer and Herr [13]. These equations are used to represent the constitutive elements of the mechanical model of the muscle tendon unit.

The resulting force of the muscle tendon unit is written as follows:

$$f_{SE} = f_t = f_m \cdot \cos(\alpha) = (f_{CE} + f_{PE} - f_{BE}) \cdot \cos(\alpha)$$

The muscle is represented with an active contractile element (CE) among others. The constitutive equation (4.1) is express as function of the dimensionless muscle length ($\widetilde{\mathbf{l_{CE}}}$) and the dimensionless shortening velocity of the muscle ($\widetilde{\mathring{\mathbf{l}}_{\mathbf{CE}}}$).

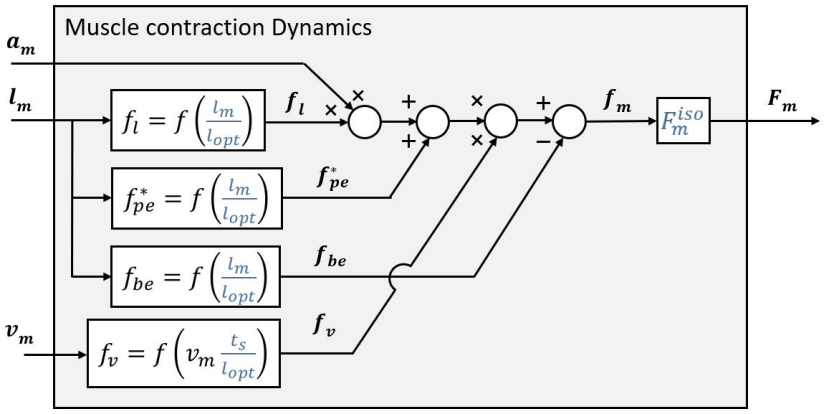

Figure 4.6: Diagram of the muscle contraction dynamic. Based on the muscular activation (a_m), the muscle length (l_m) and the shortening velocity of the muscle (v_m) the muscle force (F_m) can be found.

◇ **Contractile element CE:**
The contractile element consists of a force-length relationship equation (4.2) and a force-velocity relationship equation (4.3).

$$f_{CE} \triangleq a_m \cdot f_l(\widetilde{\mathbf{l_{CE}}}) \cdot f_v(\overset{\circ}{\widetilde{\mathbf{l_{CE}}}}) \quad \text{with} \quad \overset{\circ}{\widetilde{\mathbf{l_{CE}}}} \equiv \frac{d\widetilde{l_{CE}}}{d\tau} = \widetilde{v_{max}}^{-1} \cdot \frac{d\widetilde{l_{CE}}}{dt} \tag{4.1}$$

$$f_l(\widetilde{\mathbf{l_{CE}}}) = exp\left(c\left|\frac{\widetilde{\mathbf{l_{CE}}} - 1}{w}\right|\right) \tag{4.2}$$

where w is a parameter that denotes the half-width of the curve at $f_l = e^c = 0.05$

$$f_v(\overset{\circ}{\widetilde{\mathbf{l_{CE}}}}) = \begin{cases} \frac{1-\overset{\circ}{\widetilde{\mathbf{l_{CE}}}}}{1+K\cdot\overset{\circ}{\widetilde{\mathbf{l_{CE}}}}} & \text{for} \quad \overset{\circ}{\widetilde{\mathbf{l_{CE}}}} > 0 \\ N + (N-1)\cdot\frac{1+\overset{\circ}{\widetilde{\mathbf{l_{CE}}}}}{7.56\cdot K\cdot\overset{\circ}{\widetilde{\mathbf{l_{CE}}}}-1} & \text{for} \quad \overset{\circ}{\widetilde{\mathbf{l_{CE}}}} < 0 \end{cases} \tag{4.3}$$

◇ **Parallel elastic element PE:**
The constitutive equation (4.4) of the passive parallel elastic element (PE), is expressed as function of $\widetilde{\mathbf{l_{CE}}}$ through the strain of the CE (ε_{CE}) and $\overset{\circ}{\widetilde{\mathbf{l_{CE}}}}$. This element like the contractile one also consists of a force-length relationship (f^*_{PE}) and the force-velocity relationship is the same as CE.

$$f_{PE}(\widetilde{\mathbf{l_{CE}}}, \overset{\circ}{\widetilde{\mathbf{l_{CE}}}}) = \begin{cases} \underbrace{\left(\frac{\varepsilon_{CE}(\widetilde{\mathbf{l_{CE}}})}{\varepsilon^{ref}_{PE}}\right)^2}_{f^*_{PE}(\widetilde{\mathbf{l_{CE}}})} \cdot f_v(\overset{\circ}{\widetilde{\mathbf{l_{CE}}}}) & \text{for} \quad \varepsilon_{CE} > 0 \\ 0 & \text{for} \quad \varepsilon_{CE} < 0 \end{cases} \quad \text{with} \quad \varepsilon_{CE} = \widetilde{\mathbf{l_{CE}}} - 1 \tag{4.4}$$

◇ **Buffer elastic element BE:**

The constitutive equation (4.5) of the passive buffer elastic element (BE) is expressed as function of the strain of the BE (ε_{BE}), which is itself a function of the dimensionless muscle length ($\widetilde{l_{CE}}$).

$$f_{BE}(\widetilde{\mathbf{l_{CE}}}) = \begin{cases} \left(\frac{\varepsilon_{BE}(\widetilde{\mathbf{l_{CE}}})}{\varepsilon^{ref}_{BE}}\right)^2 & \text{for} \quad \varepsilon_{BE} > 0 \\ 0 & \text{for} \quad \varepsilon_{BE} < 0 \end{cases} \quad \text{with} \quad \varepsilon_{BE} = \widetilde{\mathbf{l_{min}}} - \widetilde{\mathbf{l_{CE}}} \tag{4.5}$$

The curves of the muscle constitutive elements when $a_m = 1$ are displayed on the Figure 4.7.

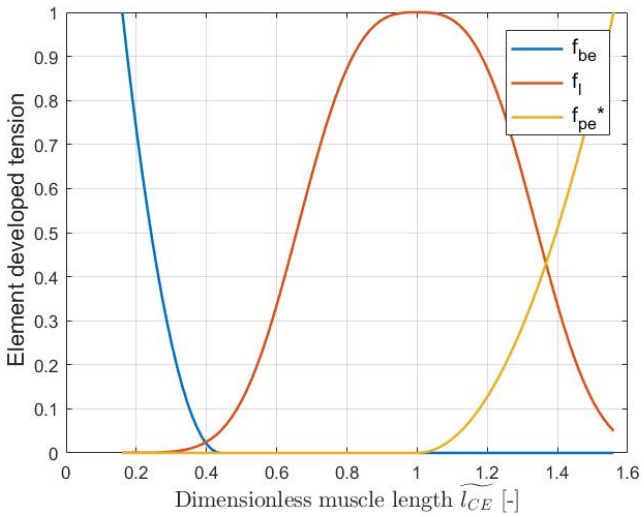

Figure 4.7: Musculotendon constitutive elements developed tension at $a_m = 1$ in function of the dimensionless muscle length $\widetilde{l_{ce}}$ (i.e. elements force at static equilibrium when muscle is fully activated).

The total force developed when the muscle is static (i.e. reach it equilibrium) and fully excited ($a_m = 1$) is the summation of the static passive force ($f_{pe}^* - f_{be}$) and the static active force ($a_m \cdot f_l$). These forces are show in Figure 4.8. The total force increases with the length until l_{opt}. Beyond l_{opt}, a passive tension altering the shape of the relationship appears. The total force decreases much more below the length $\widetilde{l_{min}}$. This is due to the passive tension of BE altering the shape of the relationship, which ensures that $\widetilde{l_{CE}}$ is not too much less than $\widetilde{l_{min}}$.

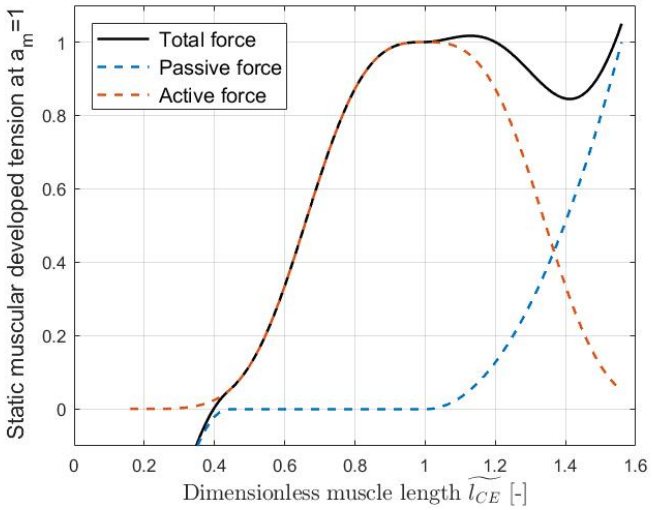

Figure 4.8: Static muscular developed tension at $a_m = 1$ in function of the dimensionless muscle length $\widetilde{l_{ce}}$ (i.e. muscular force at static equilibrium when muscle is fully activated).

The influence of a_m on f_m when $v_m = 0$ is shown on the Figure 4.9.

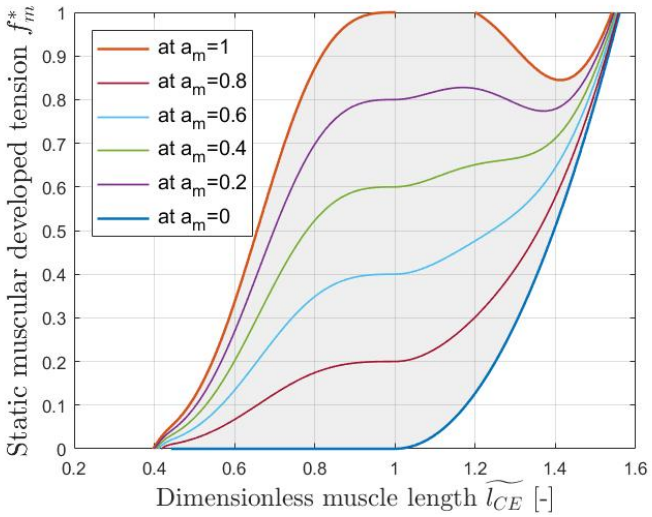

Figure 4.9: Muscular developed tension at various a_m in function of the dimensionless muscle length $\widetilde{l_{ce}}$ (i.e. muscular force at static equilibrium).

◇ **Serial elastic element SE:**

First, we will focus on the tendon part, it is represented with the passive serial elastic element (SE). It constitutive equation (4.6) is express as function of the strain of the SE (ε_{SE}), which is itself a function of the dimensionless tendon length ($\widetilde{l_{SE}}$).

$$f_t \triangleq f_{SE}(\widetilde{\mathbf{l_{SE}}}) = \begin{cases} \left(\frac{\varepsilon_{SE}(\widetilde{\mathbf{l_{SE}}})}{\varepsilon_{SE}^{ref}}\right)^2 & \text{for} \quad \varepsilon_{SE} > 0 \\ 0 & \text{for} \quad \varepsilon_{SE} < 0 \end{cases} \quad \text{with} \quad \varepsilon_{SE} = \frac{\widetilde{\mathbf{l_{SE}}}}{\widetilde{\mathbf{l_{slack}}}} - 1 \quad (4.6)$$

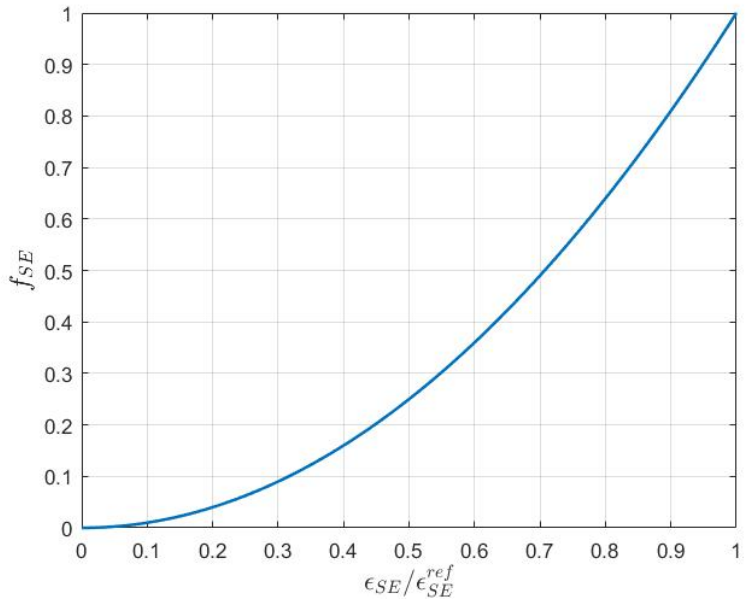

Figure 4.10: Force-strain curve of Hill Musclotendon SE element.

The values of the muscle model generic parameters used in this work are listed in the Table 4.1.

Muscle model generic parameters	
The width bell of the force-length curve	w=0.56 [-]
The reference SE strain	ε_{SE}^{ref}=0.04 [-]
The reference PE strain	ε_{PE}^{ref}=w=0.56 [-]
The reference BE strain	ε_{BE}^{ref}=w/2=0.28 [-]
The parameter related to the linear eccentricity $c = 2\frac{\sqrt{K+1}}{K}$ of force-velocity curve	K=5 [-]
The maximal eccentric force-velocity value	N=1.5 [-]
The dimensionless minimal muscle length	$\widetilde{l_{min}}$=1-w=0.44 [-]
5% of the force-length at $\widetilde{l_{min}}$	c=log(0.05) [-]

Table 4.1: The muscle model generic parameters are the same for all the muscles

4.2.4 The musculotendon propreties

This section provides details about static and dynamic properties of the dimensionless generic model of the muscle tendon unit. It also show the characteristics curves.

Tendon stiffness

The tendon stiffness links the deformation of tendon and the tendon stress. The absolute tendon stiffness is the inverse of the absolute compliance. This is an important characteristic of the muscle tendon unit. Because it describes the elasticity, the flexibility of the structure. In addition, it determines the stiffness of the joints that are affected by the muscle. It is used in Section 4.6 to estimate the musculotendon time τ^{mtu}. The tendon absolute tendon stiffness k_t and the dimensionless absolute tendon stiffness $\widetilde{k_t}$ are defined as follow.

$$\text{Absolute tendon stiffness} \quad \equiv k_t = \frac{dF_t}{dl_t} \quad \left[\frac{N}{m}\right] \tag{4.7}$$

$$\begin{aligned}\text{Dimensionless absolute tendon stiffness} \quad \equiv \widetilde{k_t} &= k_t \left(\frac{l_{opt}}{F_m^{iso}}\right) = \frac{df_t}{d\varepsilon_t} \cdot \widetilde{l_{slack}}^{-1} \propto \widetilde{l_{slack}}^{-1} \\ &= \frac{2 \cdot \varepsilon_t}{\left(\varepsilon_{SE}^{ref}\right)^2 \cdot \widetilde{l_{slack}}} = \frac{1250 \cdot \varepsilon_t}{\widetilde{l_{slack}}} \\ &= \frac{2 \cdot \sqrt{f_t}}{\varepsilon_{SE}^{ref} \cdot \widetilde{l_{slack}}} = \frac{50 \cdot \sqrt{f_t}}{\widetilde{l_{slack}}}\end{aligned}$$

Figure 4.11 shows that the stiffness of the tendon varies linearly with its deformation.

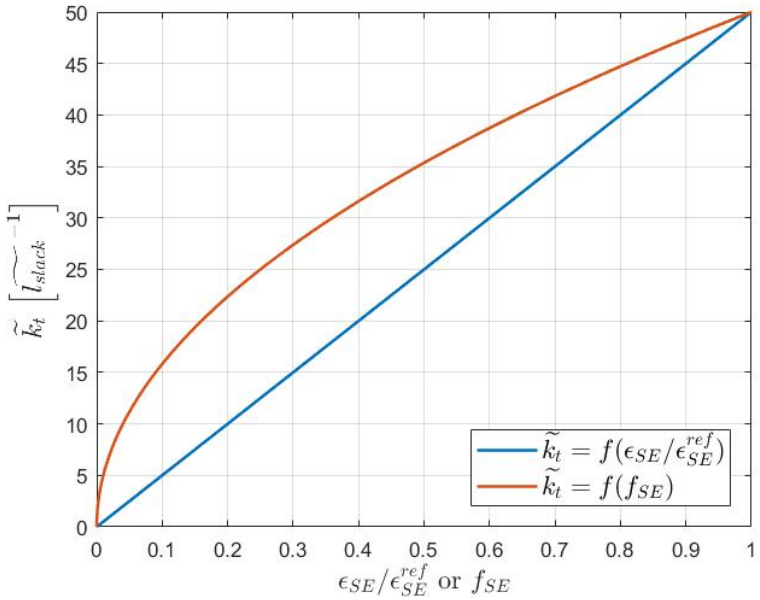

Figure 4.11: Stiffness-strain and Stiffness-Force curves of Hill Musclotendon SE element.

Estimation of metabolic energy consumption

In this part, the models for estimating muscle metabolic energy consumption available with the Hill-type muscle model are briefly presented. The approach used here is the computation of the net mechanical work of the muscle. The main advantage of this method is its simplicity. Some models such as [14] and [15] give better predictions of energy consumption. They are designed to take into account the muscle heat production during muscle action. These models add the rate of muscle heat production $\dot{\mathcal{H}}$ to the muscle power (or rate of work) $\mathcal{P} = \dot{\mathcal{W}}$ to get the total rate of metabolic energy consumption $\dot{\mathcal{E}} = \dot{\mathcal{W}} + \dot{\mathcal{H}}$.
For the moment, this would be beyond the scope of this work. But it represents a way to improve the current work by obtaining a value closer to the real metabolic cost.

The power is simply the mechanical work performed by the muscle (i.e. CE element). The power is positive when v_{ce} is negative (i.e. muscle shortening).

$$\mathcal{P}_{ce} = -F_{ce} \cdot v_{ce} \quad [W]$$

The dynamic properties like the power curve are derived with the assumption that the muscle force-length property equal to 1 ($\widetilde{l_{ce}}$ equal to 1) and on a fully activated muscle.

The shape of the $f_v - \widetilde{\mathring{l}_{CE}}$ curve determine the the mechanical work of CE. The force that a muscle can develop depends on its speed of contraction and conversely, its speed of contraction depends on the load applied (as Figure 4.12). This relationship between force and speed of contraction is hyperbolic with an upward concavity for the muscle during concentric contraction (i.e. shortening of the muscle). The eccentric contraction (i.e. lengthening of the muscle) part of the curve is hyperbolic with a downward concavity. The dimensionless power $\widetilde{p_m}$ is also plot on the Figures 4.12.

$$\widetilde{p_{ce}} \equiv \frac{\mathcal{P}_{ce} \cdot t_s}{l_{opt} \cdot F_m^{iso}} = a_m \cdot f_l \cdot f_v \cdot \widetilde{\mathring{l}_{CE}}$$

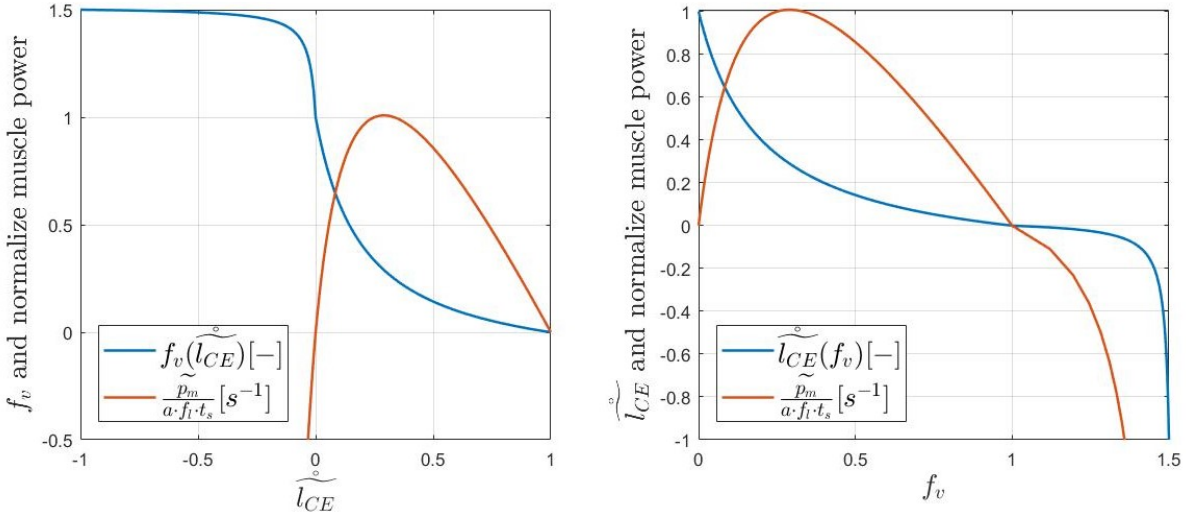

Figure 4.12: On the left there is the Velocity-Force (blue line) and Velocity-Power (orange line) curves. On the right there is the Force-Velocity (blue line) and Force-Power (orange line) curves.

The peak of power occurs at the optimal load $f_v^{opt} = \frac{\sqrt{K+1}-1}{K} \approx 0.29$ and the optimal velocity $\widetilde{l_{CE}^{opt}} = \frac{\sqrt{K+1}-1}{K} \approx 0.29$, which is consistent with respect to the value of $\approx 0.3\, l_{opt}/s$ given in [9]. We assume that the power at the power peak $\mathcal{P}_{ce}^{opt}$ divides by the muscle energy-scaling $(F_m^{iso} \cdot l_{opt})$ equals 1:

$$\frac{\mathcal{P}_{ce}^{opt}}{F_m^{iso} \cdot l_{opt}} = \frac{\widetilde{p}_{ce}^{opt}}{t_s} = 1s^{-1}$$

This results in a value of the muscle time-scaling parameter:

$$t_s = f_v^{opt} \cdot \widetilde{l_{CE}^{opt}}[s] = \left(\frac{\sqrt{K+1}-1}{K}\right)^2 = 0.0840\ s$$

These developments allow us to establish a framework and evaluate important parameters of the muscle tendon unit, such as tendon stiffness and muscle time-scaling which will be used in Sections 4.6 and 4.4 respectively.

4.3 Selection of the muscles to model

The forelimb of the bird is constituted by around 50 muscles (47 are described in the article [16]). A first step is to approximate the model of actuation (i.e. only a part of the muscles will be represented). In this case, choosing some muscles from this set of 50 muscles means forgetting other muscles. The model is composed of 10 muscles chosen in order to actuate the forelimb in a consistent way. As presented in the article [16], the muscles are assigned to four groups according to their location from the proximal to the distal one: extrinsic muscles, brachial muscles, antebrachial muscles and manual muscles. Any manual muscles were chosen due to their really small strength and the fact that they represent 0.33% of the total forelimb muscle mass. For the same criteria, the model contains:

- The four strongest extrinsic muscles which act as 2 antagonistic muscles pairs (PT-SC and SHC-CBC).

- The two strongest brachial muscles, which act as an antagonistic muscle pairs (TH-BB).

- The two strongest antebrachial muscles, which act as an antagonistic muscle pairs (EMR-FCU). ECU is then also needed because the antagonistic muscle groups is more precisely EMR-(FCU & ECU). Were EMR acts as flexor of the manus, FCU and ECU act as extensors of the manus. In addition, FCU and ECU forms also an antagonistic muscle pairs.

The last muscles chooses is TP even though it is not a strong muscle. It is a triarticular muscle which ensures geometric relation and the "rigidity" of the leading edge of the wing. It is important to note that the model do not have pronators and supinators of the antebrachial.

For each muscle, the specific set of parameters must be defined.

4.4 Numerical values of the specific parameters

In this section, the way to compute or evaluate the specific parameters for the muscle will be explained. The specific parameters are the one presented in Section 4.2.2 (F_m^{iso}, l_{opt}, t_s, $\widetilde{l_{slack}}$, α_0). The muscle mass m_{mtu} is also a useful parameter (for multi-body dynamic and metabolic aspect).

In the absence of data from the bird of interest and the incapacity to access an individual. A scaling and adjustment of data from other species need to be performed. The article [16] shows quantitative anatomical data on the muscle architecture of the forelimb (wing) of the Golden Pheasant (Chrysolophus pictus).

4.4.1 Reference muscle data set

We need to find the whole data set of the Golden Pheasant The article give m_{mtu}, l_{opt}, the belly length of the muscle l_{belly}, the muscle volume vol_{mtu}, the physiological cross-section area of the muscle PCSA and F_m^{iso}. The l_{slack} are given on the Figure 2 of the article [16] except for the pectoralis muscle (PT) and the supracoracoideus muscle (SC). An estimation is required for the missing values l_{slack}^{PT}, l_{slack}^{SC}, α_0 and t_s.

- To estimate $\widetilde{l_{slack}}$ for PT and SC, the $\widetilde{l_{slack}}$ and the ratio between the slack length and the belly length $\frac{l_{slack}}{l_{belly}}$ values from SHC and CBC (i.e. proximal muscles) are used. With the following formulation, PT and SC will have the same mean of $\widetilde{l_{slack}}$ than SHC and CBC. It maintains also the same "variation" with respect to the $\frac{l_{slack}}{l_{belly}}$ ratio (i.e. SHC for PT and CBC for SC).

$$\widetilde{l_{slack}}^{PT} = \frac{\widetilde{l_{slack}}^{SHC} + \widetilde{l_{slack}}^{CBC}}{\frac{l_{slack}}{l_{belly}}^{SHC} + \frac{l_{slack}}{l_{belly}}^{CBC}} \cdot \frac{l_{slack}}{l_{belly}}^{SHC} = 0.4462$$

$$\widetilde{l_{slack}}^{SC} = \frac{\widetilde{l_{slack}}^{SHC} + \widetilde{l_{slack}}^{CBC}}{\frac{l_{slack}}{l_{belly}}^{SHC} + \frac{l_{slack}}{l_{belly}}^{CBC}} \cdot \frac{l_{slack}}{l_{belly}}^{CBC} = 0.4910$$

- The optimal pennation angle can be obtained thanks to the formula of the physiological cross-section area of the muscle.

$$PCSA = \frac{m_{mtu} \cdot \cos(\alpha_0)}{l_{opt} \cdot \rho_m}$$

  The density of the muscle ρ_m is taken constant and equal to $1.060x10^3 kg/m^3$ for all the muscles. If the fiber is not pennate, the PCSA is equivalent to the Anatomical cross-section area of the muscle ACSA.

$$\alpha_0 = arccos\left(\frac{PCSA \cdot l_{opt} \cdot \rho_m}{m_{mtu}}\right)$$

  Three non-nulls values are obtained for the optimal pennation angle, 6.8° for TH, 13° for EMR and 10.6° for FCU. Which is consistent with the comment in the article [16]. We will need to investigate whether these angles are feasible in our model and if so, whether they have a meaningful impact (cfr Section 4.5).

- The muscle time-scaling parameter t_s is assumed as a constant and equal to $\left(\frac{\sqrt{K+1}-1}{K}\right)^2 \approx 0.0840s$ for all the muscles (cfr Section 4.2.4). By extension, the normalised maximum shortening velocity $\widetilde{v_{max}} = -t_s^{-1}[l_{opt}/s]$ is equal to $-11.9\ l_{opt}/s$, which is consistent with respect to the value of $-12\ l_{opt}/s$ assumed in [9].

4.4.2 The Bald Ibis muscle data set

Now that the whole data set of the Golden Pheasant is computed. A scaling is needed to obtain the one of the Bald Ibis. Here it is assumed that birds are following an isometric scaling. It is equivalent to the assumption of constant density.

$$\begin{aligned} Volume &\propto Mass && \Rightarrow \text{for the muscles masses } m_{mtu} \\ Area &\propto Mass^{2/3} && \Rightarrow \text{for } F_m^{iso} \text{ as } F_m^{iso} = \sigma_m^{iso} \cdot PCSA \\ Length &\propto Mass^{1/3} && \Rightarrow \text{for the length like } l_{opt} \end{aligned}$$

The dimensionless values such as $\widetilde{l_{slack}}$ and α_0 are conserved. The maximum isometric muscle force F_m^{iso} is characterised with the isometric stress under maximal activation $\sigma_m^{iso} = 3.0x10^5\ N/m^2 = 0.3MPa$ (σ_m^{iso} is assumed the same for all the muscles) and the physiological cross-section area of the muscle (PCSA). The total mass ratio between the Northern bald ibis and the Golden Pheasant used here is equal to $\frac{Mass_{NBI}}{Mass_{GP}} = 2.8436$.

Adjust l_{opt} of the data set:

Now, The muscle data set of the Northern bald ibis is completed. However, a common assumption is that l_{opt} can be reached at a certain position of the forelimb joint need to be taken in account. The value of l_{opt} must range with respect to the musculoskeletal model from $\frac{l_{mtu}^{min}}{1+\widetilde{l_{slack}}}$ to $\frac{l_{mtu}^{max}}{1+\widetilde{l_{slack}}}$.

For monoarticular muscle:

$$l_{mtu}^{max} = \|r_{ori}\| + \|r_{ins}\|$$

$$l_{mtu}^{min} = abs(\|r_{ori}\| - \|r_{ins}\|)$$

For biarticular muscle (EMR,FCU,ECU):

$$l_{mtu}^{max} = \|r_{ori}\| + \|r_{ins}\| + \|l_{Forearm}\|$$

$$l_{mtu}^{min} = max\Big(abs\big(\|l_{Forearm}\| - max(\|r_{ori}\|, \|r_{ins}\|)\big) - min(\|r_{ori}\|, \|r_{ins}\|), 0\Big)$$

For Triarticular muscle (TP):

$$l_{mtu}^{max} = \|r_{ori}\| + \|r_{ins}\| + \|l_{Forearm}\| + \|l_{Arm}\|$$

$$l_{mtu}^{min} = max\Big(abs\big(\|l_{Forearm}\| - \|r_{ins}\|\big) - \|l_{Arm}\|, 0\Big) \quad \text{for the reason that } \|r_{ori}\| = 0$$

The whole data set of the Northern bald ibis required for the muscle modelisation is completed and available in Appendix B. The values of l_{opt} and $\widetilde{l_{slack}}$ are consistent with 2 tendencies observed. There is a trend that proximal muscles have longer l_{opt} than the distal one. There is another trend that proximal muscles have smaller $\widetilde{l_{slack}}$ ratio than the distal one.

4.5 Pennation impact and model limitation

The pennation angle is defined with respect to the optimal pennation angle α_0 (see Equation (4.8)). The optimal pennation angle α_0 represents the angle when the muscle length is equal to its optimal value l_{opt}. The muscle thickness is assumed as a constant. This hypothesis and variants are compared in [11].

$$\alpha(\widetilde{l_m}) = arcsin\left(\frac{sin(\alpha_0)}{\widetilde{l_m}}\right) \tag{4.8}$$

In order to avoid reaching the singularity, it is interesting to estimate the maximum optimal pennation angle depending on the geometry and properties of the muscle. The extreme case occurs when the muscle fibers are at 90° and at their minimal length as shown in Figure 4.13 and give the Equation (4.9).

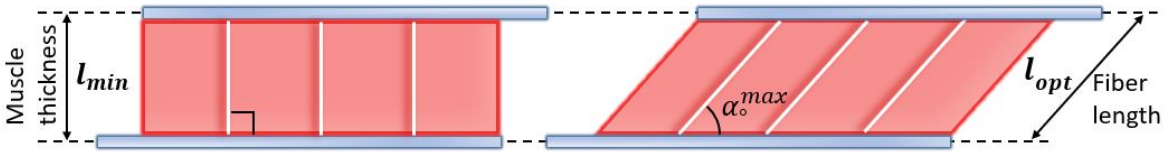

Figure 4.13: Representation of the extreme case with the singularity on the left and the optimal state (at an angle α_0^{max}), which allows reaching the singularity. The muscle are in light red and tendon are in light blue.

$$\alpha_0^{max} = \arcsin\left(\widetilde{l_{min}}\right) = 26.1° \tag{4.9}$$

The maximum possible optimal pennation angle is then equal to 26.1° for any muscles describes here. This result is consistent with the maximal value of the optimal pennation angle for real muscles, which is about 30%. This means that the pennation angle at optimal position causes few force "losses", because $\cos(26.1°) = 0.898$ (10% of the muscle force is not transmitted). The optimal pennation angles greater than $\alpha_0^{max} = 26.1°$ are rounded down to avoid the possibility of reaching the singularity.

Moreover, the optimal pennation angle under which the pennation aspect of the muscle can be neglected can also be evaluated. In Equation (4.10), λ stands for the maximum tolerated error on the "effective" muscle length l_m^{α}.

$$\alpha_0^{neg}(\lambda) = \arcsin\left(\sin\left(\arccos\left(1-\lambda\right)\right)\widetilde{l_{min}}\right) = 7.9° \text{ for } \lambda = 0.05 \tag{4.10}$$

For small optimal pennation angles (i.e. $\alpha_0 < 7.9°$), it's reasonable to assume that the pennate muscle behaviour is similar to the case with a parallel muscle. It will make at worst a 5% of error on the "effective" muscle length l_m^{α}. In other words, the effect of the pennation angle can be neglected for optimal pennation angles below 7.9°.

This allows us to ignore the pennation aspect of muscles, which have a small optimal pennation angle (i.e. $\alpha_0 < 7.9°$), without generating too much error. In our case, the muscle TH can be assume as a parallel muscle.

4.6 Musculotendon actuator dynamics rate limiting

This section is used to determine whether it is the activation dynamics or the contraction dynamics of the muscle that limits the overall response time of the muscle system. The result may vary depending on the muscle. For example, if it is the contraction dynamics of the muscle that limits the overall response time of a muscle. Then the activation dynamics of that muscle will have little impact or may be neglected.

As determined in Section 4.4 the muscle time-scaling parameter $t_s = 0.0840s$. The activation time constant is equal to 0.015 (value given in [17]).

$$\left.\begin{array}{ll} t_{act} & = 0.015s \\ t_s & = 0.0840s \end{array}\right\} \Rightarrow \text{Normalise activation time rate} \quad \equiv \tau_{act} \triangleq \frac{t_{act}}{t_s} = 0.1786 \tag{4.11}$$

As specified in [9], the musculotendon time (τ^{mtu}) can be estimate thanks to the dimensionless absolute tendon compliance. We translate this into the following expression. $\tau^{mtu} \approx$ the mean value of the tendon compliance. The absolute tendon compliance is the inverse of the absolute stiffness. The tendon absolute tendon stiffness k_t and the dimensionless absolute tendon stiffness $\widetilde{k_t}$ are defined in Section 4.2.4

$$\text{Normalise musculotendon time rate} \quad \equiv \tau_{mtu} \approx \int_0^1 \widetilde{k_t(f_t)}^{-1} df_t = \frac{\widetilde{l_{slack}}}{25}. \tag{4.12}$$

Indeed, The tendon can be classified as very long, intermediate or very short with respect to their $\widetilde{l_{slack}}$ ratio:

$$\frac{\tau_{mtu}}{\tau_{act}} \approx \frac{2}{9} \cdot \widetilde{l_{slack}} \begin{cases} \geqslant 3 & \text{very long tendon:} \quad \widetilde{l_{slack}} \geqslant 13.5 \\ \in]0.33, 3[& \text{intermediate tendon:} \quad \widetilde{l_{slack}} \in]1.5, 13.5[\\ \leqslant 0.33 & \text{very short tendon:} \quad \widetilde{l_{slack}} \leqslant 1.5 \end{cases} \tag{4.13}$$

A stiff actuator is represented with a small $\widetilde{l_{slack}}$ ratio (i.e. $\leqslant 1.5$). It does not influence that much the model properties (i.e. it does not stretch that much). On the other hand, a highly compliant actuator is represented with a high $\widetilde{l_{slack}}$ ratio (i.e. ≥ 13.5).

For the set of muscle selected, 2 muscles (EMR and ECU) are considered with intermediate tendon. The remaining part have very short tendon (i.e. stiff tendon). It means that for 8 out of 10 muscles the activation dynamic is not negligible and represents the major part of the muscle response time.

As a consequence of these results, the activation dynamic of the muscle must be well described and modeled (cfr Section 4.7).

4.7 Activation dynamics of the muscle

The objective of this section is to describe the information transmission characteristics of the central nervous system to the muscles.

The neural stimulation is the main input triggering muscle actuation. The neural stimulation (s_m) is filtered by a low pass filter and gives the muscular activation (a_m), which will activate the muscle. The activation dynamics is modeled with a differential equation as Equation (4.14). Its computation depends on the two inputs the neural stimulation (s_m) and the muscle activation (a_m). a_m is the response of the low-pass filter capturing the excitation-contraction (EC) coupling, corresponding to the input s_m.

$$\dot{a}_m(t) = f(a_m, s_m) \tag{4.14}$$

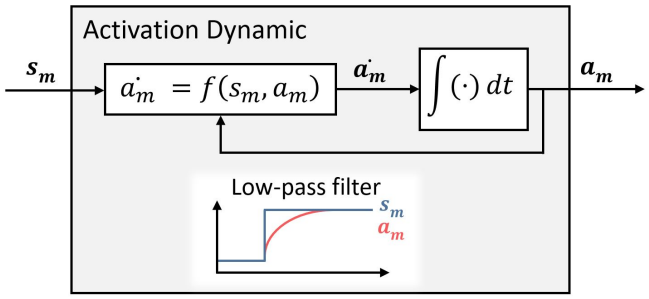

Figure 4.14: Diagram of the muscle activation dynamic.

These signals are both bounded between 0 and 1:

- 0 stand for deactivated (a_m=0), unexcited (s_m=0) state.
- 1 stand for fully activated (a_m=1), totally excited (s_m=1) state.

To describe the muscle delay activation, a first-order low-pass filter (as Equation (4.15)) is a good start.

$$\dot{a}_m(t) = \frac{s_m - a_m}{t_{act}} \tag{4.15}$$

But in fact, an important aspect of the activation dynamics is that the time rate constant of activation is greater than the one of deactivation (i.e. when the muscle is unexcited) (see Figure 4.15), as stated notably in articles [9] and [17].
Hence, a low pass filter with a variable rate is chosen to better capture the excitation-contraction coupling. In other words, to better characterise the activation dynamics. First, a differential equation like in Zajac,1989 [9] is taken.

$$\dot{a}_m(t) = \frac{s_m - \Big(\beta + (1-\beta)s_m\Big)a_m}{t_{act}} \qquad with \quad \beta \equiv \frac{t_{act}}{t_{deact}} \tag{4.16}$$

- $t_{act} \equiv$ muscle activation time constant when muscle is fully excited
- $t_{deact} \equiv$ muscle activation time constant when muscle is unexcited

The low-pass filtering characteristics are set to match those of the activation dynamics thanks to β (the ratio between t_{act} and t_{deact} of the muscle). The coefficient β is a fixed parameter of the muscle bounded between 0 and 1. It describes the linear evolution of the time rate with respect to s_m. The case $\beta = 1$ is the classical low-pass filter like in Equation (4.15). The muscle delay activation is therefore constant and equal to t_{act} for $\beta = 1$.

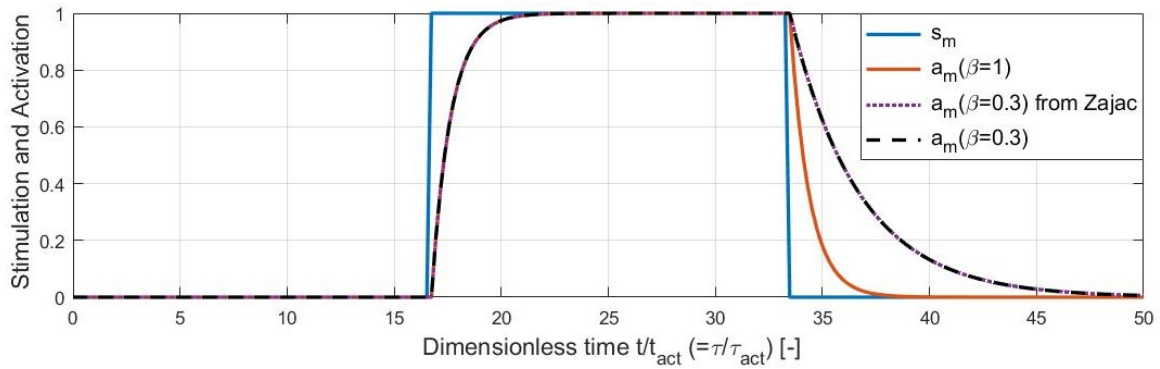

Figure 4.15: Impact of the parameter β on the EC dynamics: neural stimulation (blue line), Equation (4.15) (orange line), Equation (4.16) (purple dotted line) and Equation (4.18) (black dashed line). For this unitary neuronal stimulation the purple dotted line is overlapped with the black dashed line.

The differential equation (4.16) exhibits an undesired behaviour for low frequencies (i.e. below the activation frequency $f_{act} = t_{act}^{-1}$). It can be clearly seen at the equilibrium for $s_m \in]0, 1[$.

$$(4.16) \Rightarrow \dot{a}_m(t) = 0 \Leftrightarrow a_m|_{eq} = \frac{s_m}{\beta + (1-\beta)s_m} > s_m \quad \forall\ \beta < 1\ ,\ \ s_m \in]0,1[\tag{4.17}$$

Indeed, according to Equation (4.17) this model always overestimates the stimulation that is send to the muscle and then the equilibrium occurs at a higher value. For example, at a constant stimulation of 0.5, the activation will reach 0.77 (with β=0.3) as shown in Figure 4.16. Therefore, to correct this behavior, a second model whose equilibrium is established when $a_m = s_m$ is built.

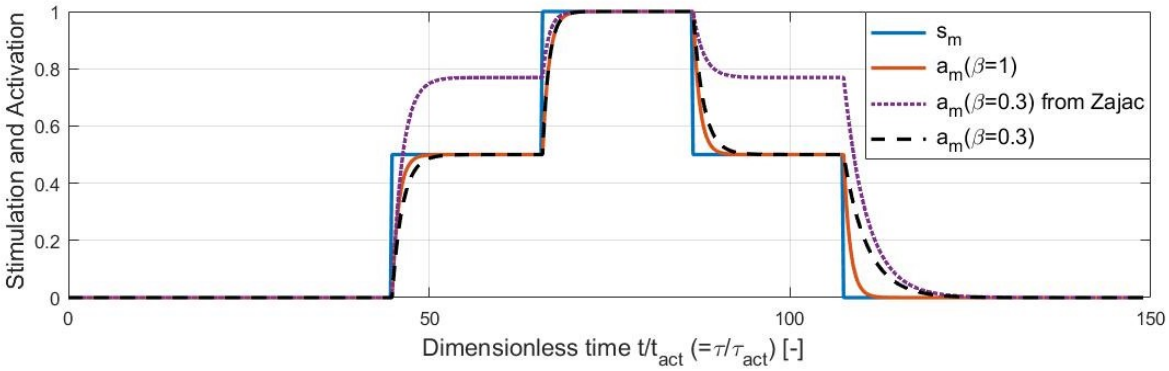

Figure 4.16: Comparison of our corrected model with respect to the one of Zajac: neural stimulation (blue line), Equation (4.15) (orange line), Equation (4.16) (purple dotted line) and Equation (4.18) (black dashed line)

We want to have a similar equilibrium as in Equation (4.15) $a_m|_{eq} = s_m$ and keep the linear variation of the rate. The Equation (4.18) perfectly achieves this goal.

$$\dot{a}_m(t) = \frac{\Big(\beta + (1-\beta)s_m\Big).(s_m - a_m)}{t_{act}} \tag{4.18}$$

To corroborate our comments, we made Bode diagrams of the Zajac's model and our modified model linearised at s_m= 1, 0.5 and 0. As illustrated in Figure 4.17, unlike our model, the Zajac's model exhibits a magnitude of the frequency response shift , when $s_m \neq 1$. This demonstrates the overestimation nature of the Zajac's model. Nevertheless, the phase shift is identical for both models. It means that the linear varying behaviour of the cutoff frequency is preserved.

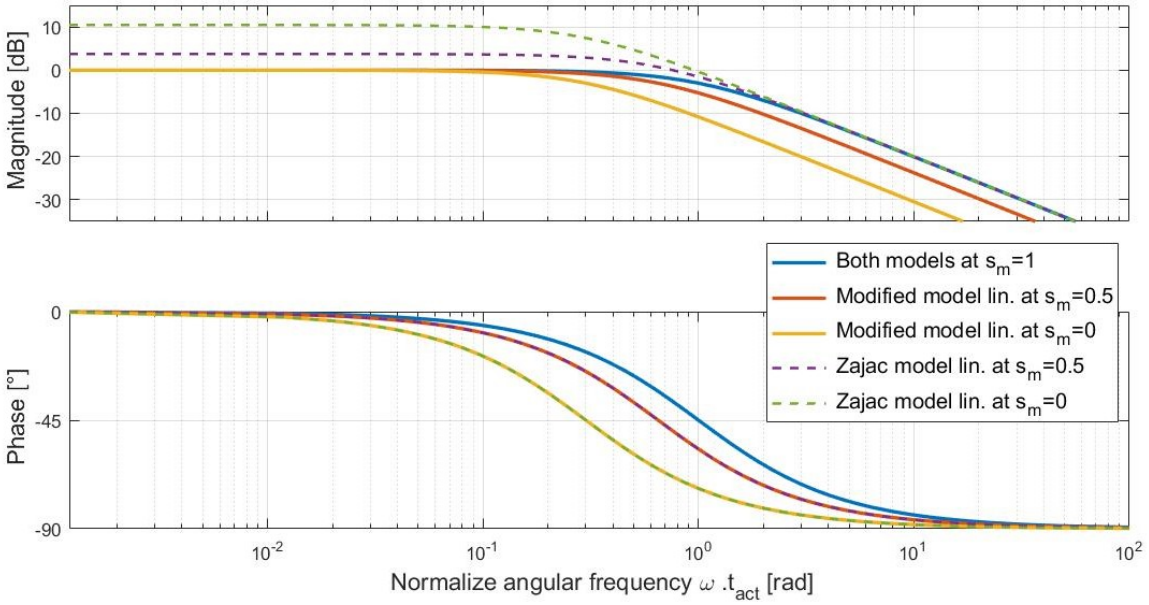

Figure 4.17: Bode diagrams of the linearised models of Zajac and the modified one at $s_m = 1, 0.5, 0$

Moreover, a zero muscle activation must be avoid, when the value of f_v is calculated in order to deduce the muscle velocity. More precisely, we have to deal with the problem of the inversion of the muscle force-velocity relation f_v.

$$\frac{f_m(l_{mtu}, \widetilde{l_{CE}}) + f_{be}(\widetilde{l_{CE}})}{a_m \cdot f_l(\widetilde{l_{CE}}) + f_{pe}^*(\widetilde{l_{CE}})} = f_v(\dot{\widetilde{l_{CE}}}) \Rightarrow \dot{\widetilde{l_{CE}}} \tag{4.19}$$

$$\text{if} \quad \widetilde{l_{CE}} < 1 \text{ and } a_m = 0 \quad \text{then} \quad (4.19) \Rightarrow \frac{f_m(l_{mtu}, \widetilde{l_{CE}}) + f_{be}(\widetilde{l_{CE}})}{0} = f_v(\dot{\widetilde{l_{CE}}})$$

Two solutions are available to us. On the one hand, a solution is to impose a lower bound on the neural stimulation being the basal neural activity (i.e. the minimum muscle stimulus s_m^{min}). On the other hand, another solution is to add an extra term to the activation dynamic to impose a lower bound to the muscle activation (i.e. the basal muscle activity a_m^{min}), as used in [18].

The extra term was modified here to have the equilibrium at $a^m|_{eq} = s^m$ for $s_m = 1$.

$$\dot{a}_m(t) = \frac{\Big(\beta + (1-\beta)s_m\Big).(s_m - a_m) + a_m^{min} \cdot \beta \cdot (1 - s_m)}{t_{act}} \tag{4.20}$$

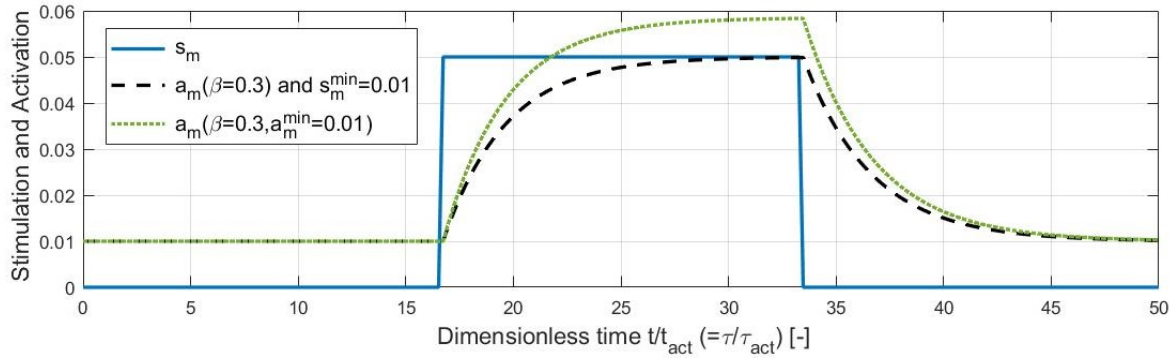

Figure 4.18: Models responses for small neural stimulation: neural stimulation (blue line), Equation (4.18) (black dashed line) and Equation (4.20) (green dotted line)

For now, we choose the first solution. Because the second one has a very slight overestimation of the muscle activation (i.e. less than one percent of overestimation) and we have no counter indication for the assumption on s_m. This choice depends on the validity of the hypothesis that neural stimulation has a minimal threshold.

All activation dynamics equations provided in this section can be nondimensionalised thanks to the muscle dimensionless time ($\tau = t/t_s$). We end up with the dimensionless constant of activation when the muscle is fully excited (τ_{act}) and the unexcited one as well (τ_{deact}). For instance, equation 4.18 becomes:

$$\mathring{a}_m(\tau) = \frac{\Big(\beta + (1-\beta)s_m\Big).(s_m - a_m)}{\tau_{act}}$$

4.8 Implementation of the muscle model simulation

At each time step of the simulation, the steps II to VI are made for the transformation of neural stimulation into musculotendon force. The first step is used to initialise the start of the simulation.

I. Initialisation of the inital values for l_{mtu}, the muscle length l_m, s_m and a_m.

II. Updating the musculotendon force $F_t = f_{SE}(l_{mtu}, l_m)$. Derive the muscle force $F_m = f(f_t, l_m)$ and also the forces of the internal elements of the muscle: the static force of the parallel element f^*_{PE} and the force of the buffer element f_{BE}.

III. Updating the force-length relationship f_l and the force-velocity relationship f_v.

IV. Updating the shortening velocity of the muscle length such that $v_m = f(f_v)$ (i.e. inverting the muscle force-velocity relation f_v).

V. Time integrating the shortening velocity of the muscle length to update l_m.

VI. The values of l_{mtu} and v_{mtu} are updated thanks to the MBS solver (with respect to the external forces F_{ext} and the internal one F_t). s_m is also updated with the neural part of the simulator, which permits to update the value of a_m.

Now, the simulation progresses through the iteration of the step II to VI until the end of the simulation time.

Steady-state approximations

In Section 4.6, the importance of the activation dynamics compared to the contraction dynamics of the muscle has been highlighted. As 8 out of 10 tendons are stiff (i.e. their contraction dynamics are faster than the activation dynamics), it is interesting to consider the hypothesis that the muscle reaches its steady state value l_{ce}^{*} (i.e. v_{ce}=0). This means neglecting the response time of the muscle contraction compared to the one of the activation dynamics. A relation between l_{ce}^{*}, l_{mtu} and a_m is established.

$$v_{ce} = f(l_{mtu}, l_{ce}^{*}, a_m) = 0 \quad \Rightarrow \quad l_{ce}^{*} = f(l_{mtu}, a_m) \tag{4.21}$$

As indicated in [19]: *"The muscle dynamics is mainly related to the computation of the speed v_{ce} of the CE part. [...] Here, we assume that the values of l_{mtu} and a_m are kept constant during each controller step call. This assumptions relies on the fact that the dynamics and rules governing l_{mtu} and a_m are much slower than the ones acting on l_{ce}.[...] Using a too large integration time step, [...] the sign of v_{ce} is reversed [at each time step][...] resulting in the oscillations of l_{ce} around its steady-state value l_{ce}^{*}. This indicates that the dynamics governing l_{ce} are so fast that it could potentially be neglected."*

This means replacing steps III to V by a single step that consists of calculating the steady-state value l_{ce}^{*} (for stiff muscle). This will reduce the computational cost and speed up the computation time. This also suppresses oscillations around the equilibrium state if the integration time step is too large.

The thesis [19] proposes and compares 3 methods to get l_{ce}^{*}:

- The values of l_{ce}^{*} are evaluated for a meshgrid of l_{mtu} and a_m, providing a look up table (LUT). The value of l_{ce}^{*} for any new l_{mtu} and a_m is then interpolated from the four closest point in the LUT.
- The LUT is used to derive a third-order polynomial approximation (TOP), computing l_{ce}^{*}.
- A Newton-Raphson scheme (NRS) is applied on the function 4.21, in order to finds its stable equilibrium, corresponding to l_{ce}^{*}.

We motivate our choice of the LUT method based on the arguments and results mentioned in [19]: *"Finally, the Look Up Table (LUT) method was the most reliable.[...] Globally, the curves fitting with the reference signals appeared to be quite accurate, in particular for the LUT method."*

However, Equation (4.21) representing the musculotendon contraction of the physical model is different for each muscle and thus requires storing one LUT for each muscle. In contrast to this thesis, we realise one and only one LUT valid for any muscle. This is the LUT of the muscle contraction dynamics for the dimensionless model (Equation (4.22)).

$$\widetilde{l_{ce}}^{*} = f(f_m^{*}, a_m) \tag{4.22}$$

The inherent consequence of this formalism is that it does not take into account the influence of pennation and the tendon compliance. These two aspects must be done aside (like in the full dynamics). There is therefore a trade-off between the memory cost and the computational efficiency to be done.

The LUT of the normalised static muscle force f_m^* as a function of a_m and $\widetilde{l_{ce}}^*$ developed here is shown in Figure 4.19. It is generated in the preprocessing before the simulation.

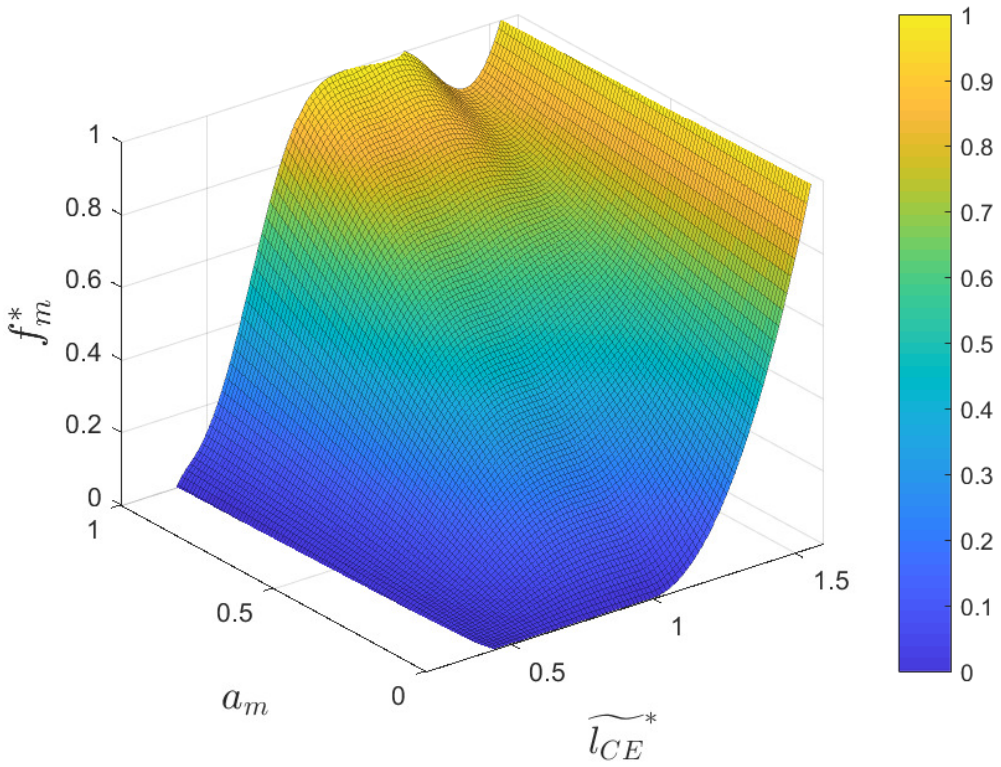

Figure 4.19: Look up table of the muscle contraction dynamics for the dimensionless model.

4.9 Conclusion

In the present work, we obtained a phenomenological model of the muscle (i.e. a Hill-type muscle model with pennation). The musculotendon specific parameters and the dimensionless model were performed and justified by a dimensional analysis. The tendon stiffness was determined in accordance with the musculotendon model. We have described our approach for evaluating the energy consumed to actuate the muscles. We have developed an original method to calculate the muscle time-scaling parameter based on the muscle force-velocity relationship that is in agreement with the empirical values provided in the literature.

We select a set of 10 muscles bases on their characteristics and the joints to which they are related. We provide an original contribution, namely the global scaling procedure of muscle parameters for any bird species. We made sure to avoid internal muscle singularities and to determine the significance of muscle pennation.

We have given particular attention to the activation dynamics, which turns out to be decisive among the majority of considered muscles, by adapting Zajac's exitation-contraction dynamics equation to ensure convergence to the desired equilibrium state and also manages the inversion of the force-velocity relationship.

We have also developed our own LUT that is valid for all muscles and can be used to approximate the muscle contraction dynamics for stiff muscles.

In this chapter, we have discussed about each of the elements. Figure 4.20 revisits Figure 4.1 and gives a graphical representation of the computational process that is hidden behind each of these blocs, according to the developments made in this chapter. We understand now what is behind every one of these elements, their importance, and how they interact together to allow us to determine the internal musculotendon forces.

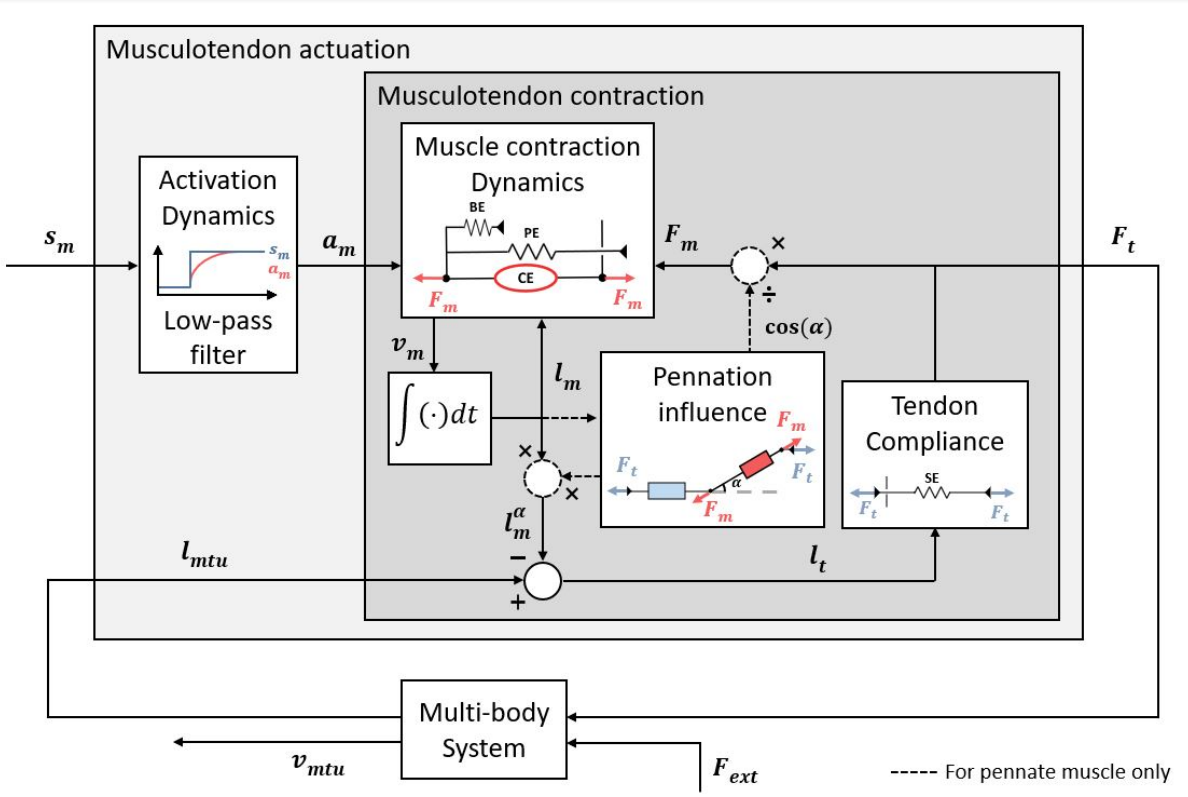

Figure 4.20: Architecture of the muscle module code. The neural controller generates the neural stimulation (s_m) that excites the musculotendon unit by a muscular activation (a_m). The musculotendon unit produces force (F_t) depending on a_m and the musculotendon length (l_{mtu}). F_t actuates the skeleton thanks to the resulting joint torques.

CHAPTER 5

Level Flapping Flight

In this work, we choose to block the pitch angle. The 2 other degrees of rotation and the transverse translation are not blocked. But they will be null by a symmetry of the wings kinematics and a wind speed vector in the same symmetry plane .

5.1 Wing kinematics

Before calculating the aerodynamic forces, the muscular forces and controlling the musculoskeletal system of the bird, it is necessary to prescribe a flight kinematics. We adopt the same formalism as in [2] to describe the kinematics of the wing. The 7 DOFs of the wing are described by harmonic trajectories.

For a joint angle i, the harmonic trajectory ($q_i(t)$) is:

$$q_i(t) = q_{0,i} + A_i \cdot sin(\omega t + \phi_{0,i})$$

With the amplitude A_i, the mean value $q_{0,i}$, the phase $\phi_{0,i}$ and $\omega = 2\pi T_{flight}^{-1}$. T_{flight}^{-1} is the flapping frequency, it is identical for all wing joint.

Table 5.1: Summary of the kinematic parameter relationship with 4 independent parameters (in red).

	Shoulder x	Shoulder y	Shoulder z	Elbow z	Elbow y	Wrist x	Wrist z
Mean q_0	0	$q_{0,s,y}$	$q_{0,s,z}$	$-0.75A_{s,x}$	0	0	$0.75A_{s,x}$
Amplitude A	$A_{s,x}$	$A_{s,y}$	$A_{s,x}/2$	$-q_{0,e,z}$	$0.083A_{s,x}$	0	$q_{0,w,z}$
Phase ϕ_0	0	$-\pi/2$	$-\pi/2$	$\pi/2$	$-\pi/2$	0	$-\pi/2$

5.2 Open-loop model of flapping flight

We obtain empirically the set of parameters for a flight at 15m/s:

- Amplitude of flapping motion $\equiv A_{s,x} = 27.5°$
- Amplitude of pitching motion $\equiv A_{s,y} = 10°$
- Mean value of pitching motion $\equiv q_{0,s,y} = 4°$

- Mean value of sweeping motion $\equiv q_{0,s,z} = 10°$

Now we impose the kinematics of the wing in open loop and we obtain the resultant of the aerodynamic forces of a wing in the frame of the Earth (which is the same as that of the body of the bird in this case) in Figure 5.1.

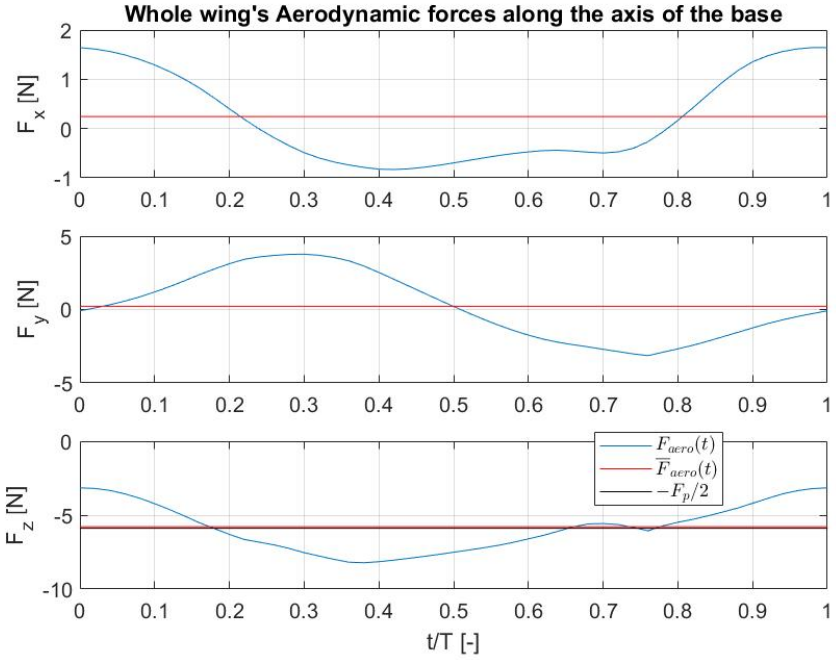

Figure 5.1

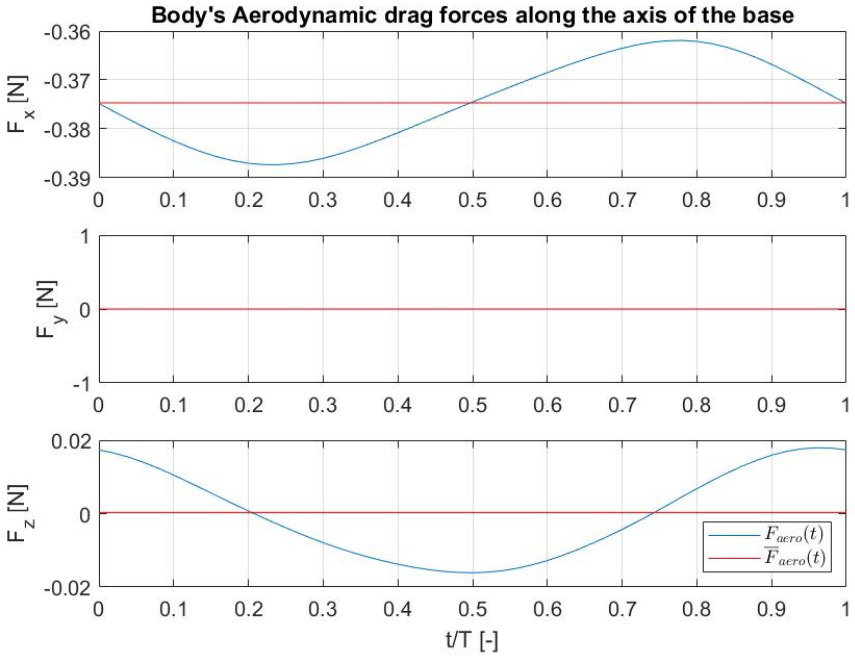

Figure 5.2

To move forward at constant speed along x_e, the resultant of the aerodynamic forces of the wings along x_e must compensate the drag of the body along x_e. To be in level

flight, the velocity according to z_e must be zero, the resultant of the aerodynamic forces of the wings according to z_e must compensate the drag of the body according to z_e and the weight of the bird. The lateral balance is ensured by the symmetry of the wings. The bird's body drag aerodynamic forces along the frame of the Earth is shown in Figure 5.2.

The results are shown in Figure 5.3 and Figure 5.4 in a version normalised by the bird's weight (and the average chord for the pitching moment).

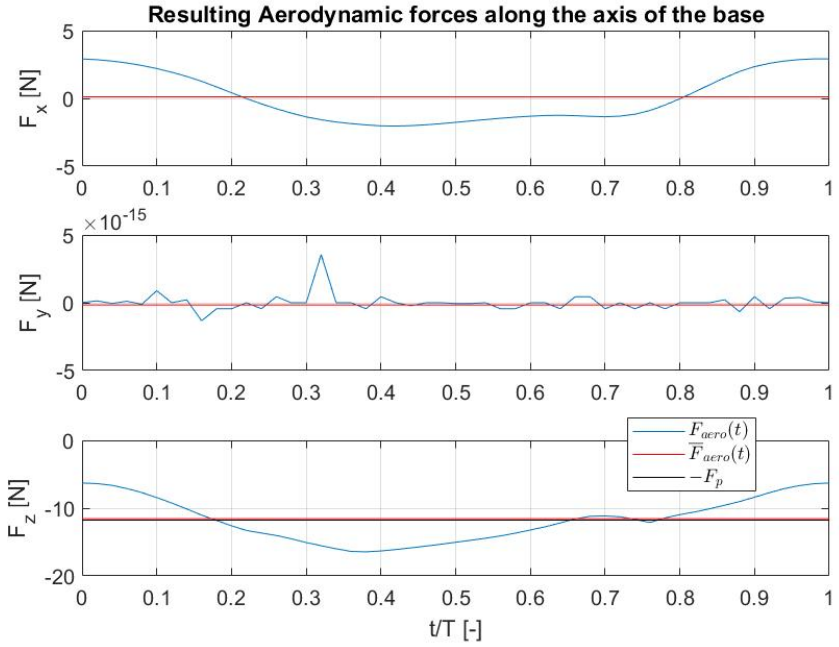

Figure 5.3

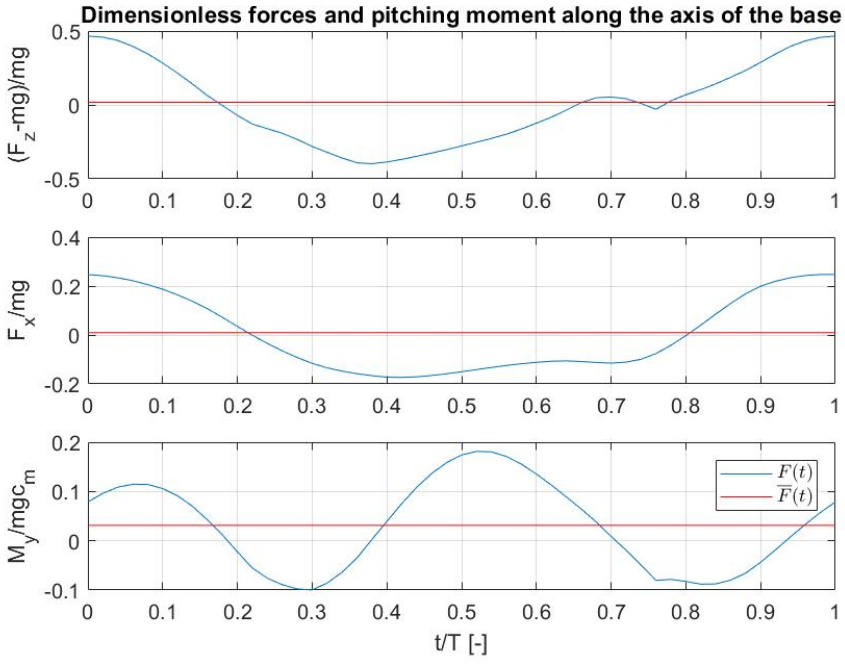

Figure 5.4

We see that the forces are well balanced. But not the pitching moment, that's why the pitch angle is fixed constant for now.

Figures 5.5 and 5.6 are respectively the phase diagram of the acceleration, velocity of the bird. The acceleration over one flapping period is indeed zero.The average horizontal velocity is 15.08m/s and the average vertical velocity is 0.0128m/s (i.e. the bird descends a little bit). On Figure 5.7, there is the flight path over a flapping period.

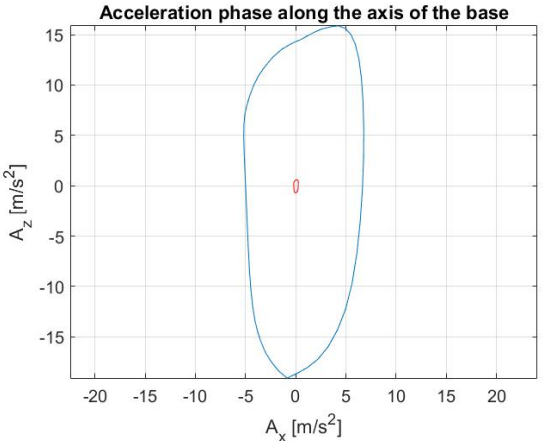

Figure 5.5

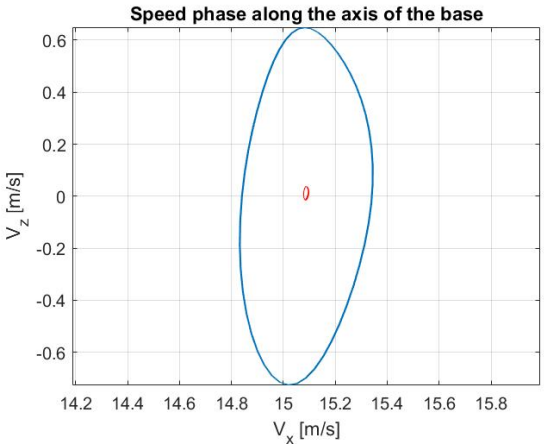

Figure 5.6

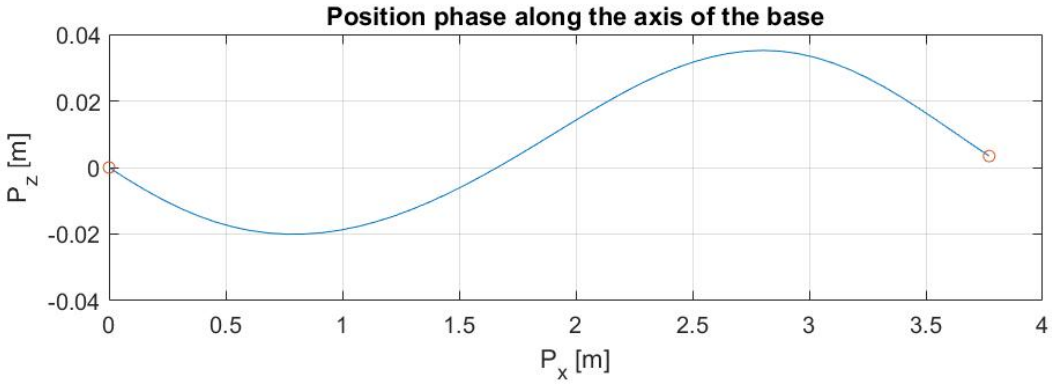

Figure 5.7

CHAPTER 6

Conclusions and future work

6.1 Conclusions

This work and the associated code can be adapted for any type of bird by changing the numerical values.

Although the parts about the over-actuation solving problem and the Reflex-based approach are not developed here. They are already investigated in the code.

Such a tool can allow the creation of bio-inspired bird-like robots. For example, roboticists at the University of Twente (Netherlands) have developed a realistic robotic bird that patrols along the landing strip at Edmonton International Airport (Canada) to scare away real birds. It is involved in a large-scale drone project in Edmonton, which will not only keep planes safe, but also observe wildlife, inspect buildings and take 3D measurements.

Figure 6.1: RoBird (a bird-like drone) is produced by Clear Flight Solutions (a spin-off from the University of Twente)[20]

In addition, this tool also allows the study or development of new ways of aerial locomotion with variable geometry aircraft, which is able to change its physical configuration during flight. These aircrafts offer a better maneuverability for stabilisation a bio-inspired

control can be investigated.

The approach and methodology developed here, can be used as a starting template in the modeling of flight or swimming locomotion of animals and insects such as a ray, a bee, etc.

Figure 6.2: On the upper left: a spotted eagle ray (Aetobatus ocellatus)[21], On the lower left: a spotted eagle ray (Aetobatus narinari)[22] and on the right a foraging bee [23]

Ethics statement: This study was carried without any experimentation on real birds.

6.2 Future work

Makes a comparison of several optimisation methods for estimating muscle forces in a level flapping flight approach using inverse dynamics and direct dynamics approaches. Shows the application of the methods proposed in this work to build a reflex and CPG based approach to control muscle activation.

The bird's tail can also be added in the modeling as it contributes to lift generation, maneuvers and active stabilisation during flight.

The article [24] highlights an unexpected ways in which birds can use their tails to generate extra lift and reduce drag while gliding. As expected, the researchers saw vortices spinning down from the wing tips. This helps provide lift. But the swirling bubbles (shown in Figure 6.3) revealed a second pair of vortices swirling in the air behind the bird coming down from the tail. These also generate lift and because they come from the tail, the lift is spread more evenly over the bird's body, which is reducing the overall drag.

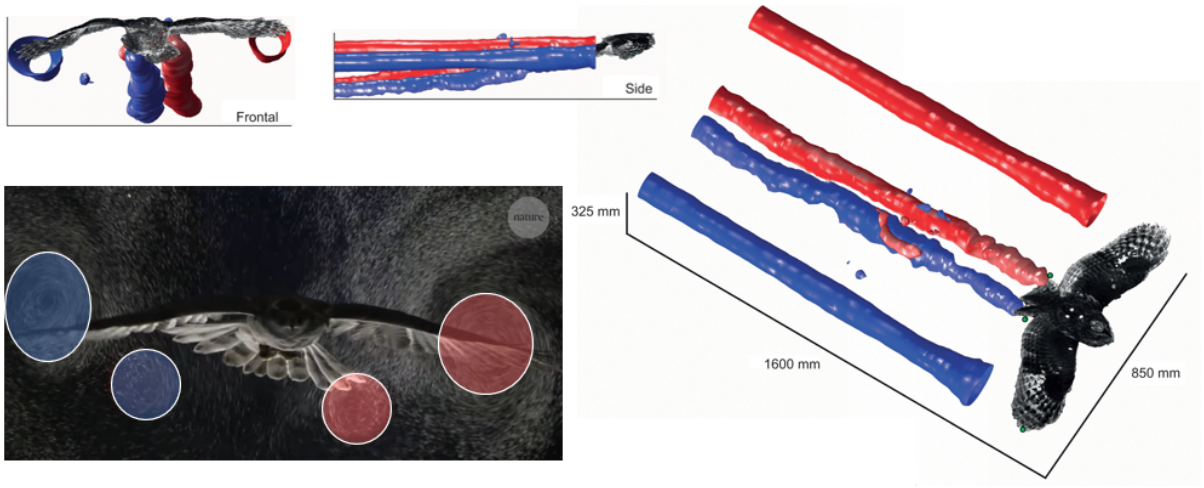

Figure 6.3: These images show the wing and tail tip vortices. On the lower left: a real owl bursting through a cloud of bubbles (adapted from [25]) and on the right and upper left: the numerical simulation results of the same vortices (adapted from [24])

It may also be interesting to discretise the degree of transverse rotation of the forearm to better represent the homogeneous torsion along the forearm. For example, this can be done by sectioning the forearm segment into sub-segments.

The aerodynamic code can be improved to calculate the wake and model the feathers (as done by Victor Colognesi in [2]). This will allow to evaluate the impact of the bird on the surrounding fluid and vice versa. As well as, the impact and the study of the flights in cluster and V formation. The V formation flocks are typically seen in association with migration, because it is a cooperative aerodynamic formation. While cluster or mixed flocks is important in safety from predation and foraging benefits.

The evaluation of the energy consumed can be improved by taking into account the heat produced by the activation of the muscles.

Appendix A

Numerical values of the bodies properties

- The total mass of the bird: $M_{Tot} = 1.2kg$
- The length of the bird (without its beak): $l_B = 0.6127m$
- The inter-coracoid space: $l_{ICS} = 0.092m$
- The wingspan: $WS = 1.354m$
- The wing area: $WA = 0.242m^2$
  (the aspect ratio $\equiv Ar \triangleq \frac{WS^2}{WA} = 7.531$ and the standard mean chord $\equiv SMC \triangleq \frac{WA}{WS} = 0.1793m$)
- The transverse length of the arm sections: l_A= humerus length $= 0.134m$
- The transverse length of the forarm sections: l_F= ulna length $= 0.162m$
- The transverse length of the hand sections: l_H=carpometacarpus length+primary feather length $= 0.084 + 0.265 = 0.349m$
- The chord at the joint and wingtip: $c_1 = 0.22m$, $c_2 = 0.2m$, $c_3 = c_2$ and $c_4 = 0.088m$
  The wingtip chord is obtained by matching the area of the chord distribution to the wing area WA:

$$\begin{aligned} c_4 &= \frac{WA - c_1(l_A + l_{ICS}) - c_2(l_A + l_F) - c_3(l_F + l_H)}{l_H} \\ &= \frac{WA - c_1(l_A + l_{ICS}) - c_2(l_A + 2l_F + l_H)}{l_H} \quad \text{with } c_3 = c_2 \end{aligned}$$

- The position of the centers of gravity of the wing sections along the y axis within their wing segment frame for the right wing:
  $GC_A = 0.065078m$, $GC_F = 0.081000m$ and $GC_H = 0.131372m$
- As specified in article [16], the mass of the PT muscle (m^{PT}_{mtu}) represents 55.86% of the wing mass. The value of the PT muscle mass is provided in the Appendix B:
  $M_{wing} = 146.8g$ and $M_{body} = 906.4g$
- The densities of the bird: $\rho_{wing} = \frac{M_{wing}}{V_{wing}} = 152.082kg/m^3$ $\rho_{body} = \frac{M_{body}}{V_{body}} = 333.878kg/m^3$

- The masses of the wing sections: $M_A = 42.573g$, $M_F = 47.963g$ and $M_H = 56.226g$
- The inertia matrix of the bodies at their center of gravity:

$$\underline{\underline{I_{body}}} = 10^{-3}\begin{bmatrix} 0.767 & 0 & 0 \\ 0 & 17.4 & 0 \\ 0 & 0 & 17.4 \end{bmatrix} kg \cdot m^2 \qquad \underline{\underline{I_F}} = 10^{-3}\begin{bmatrix} 0.107 & 0 & 0 \\ 0 & 0.071 & 0 \\ 0 & 0 & 0.174 \end{bmatrix} kg \cdot m^2$$

$$\underline{\underline{I_A}} = 10^{-3}\begin{bmatrix} 0.066 & 0 & 0 \\ 0 & 0.07 & 0 \\ 0 & 0 & 0.131 \end{bmatrix} kg \cdot m^2 \qquad \underline{\underline{I_H}} = 10^{-3}\begin{bmatrix} 0.49 & 0 & 0 \\ 0 & 0.055 & 0 \\ 0 & 0 & 0.541 \end{bmatrix} kg \cdot m^2$$

The total mass of the bird and the length of the bird come from [26]. The inter-coracoid space length, humerus length, ulna length, carpometacarpus length, primary feather length, wingspan and wing area values for the northern bald ibis (geronticus eremita) come from the master thesis [5].

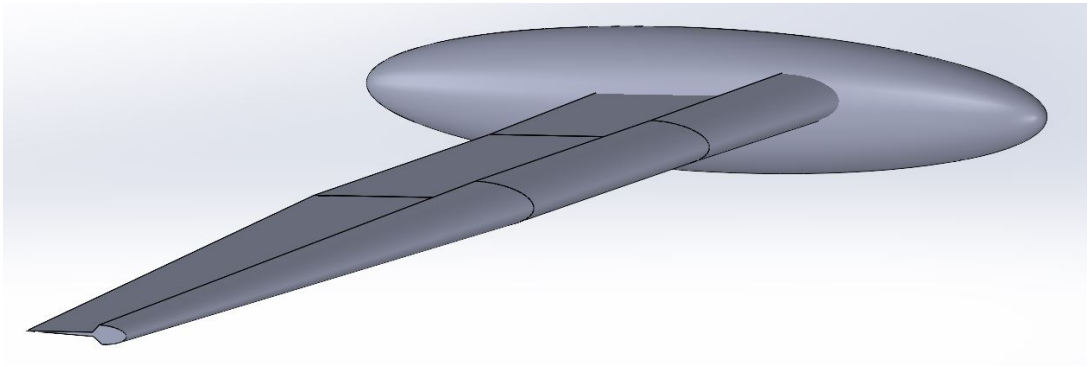

Figure A.1: Representation of the bird's body and right wing sections using Solidworks.

Appendix B

Muscle tendon parameters

The fixed MTU parameters of the 10 muscles for IbisCUS are reported in this table.The values of $\vec{R_{ori}}[m]$ and $\vec{r_{ins}}[m]$ were extracted from the master thesis [5]. The othres muscles parameter were estimated with the data from [16] as explained in Section 4.4.

	$F_m^{iso}[N]$	$l_{opt}[mm]$	$\widetilde{l_{slack}}[-]$	$\alpha_0[^\circ]$	$\vec{R_{ori}}[m]$	$\vec{r_{ins}}[m]$	$m_{mtu}[g]$
PT	671.495	47.1132	0.4462	0	$\begin{pmatrix} -0.036 \\ 0 \\ 0.091 \end{pmatrix}$	$\begin{pmatrix} 0 \\ 0.04 \\ 0 \end{pmatrix}$	81.9810
SC	218.681	35.9644	0.4910	0	$\begin{pmatrix} 0.032 \\ 0 \\ -0.075 \end{pmatrix}$	$\begin{pmatrix} 0 \\ 0.04 \\ 0 \end{pmatrix}$	24.1564
SHC	97.0134	36.8737	0.3707	0	$\begin{pmatrix} -0.86 \\ 0.027 \\ -0.021 \end{pmatrix}$	$\begin{pmatrix} 0 \\ 0.04 \\ 0 \end{pmatrix}$	7.8796
CBC	64.1364	14.6066	0.5664	0	$\begin{pmatrix} 0.026 \\ 0.03 \\ 0.028 \end{pmatrix}$	$\begin{pmatrix} 0 \\ 0.04 \\ 0 \end{pmatrix}$	3.1308
TH	61.5632	41.1307	1.4951	6.924	$\begin{pmatrix} -0.012 \\ 0.019 \\ 0 \end{pmatrix}$	$\begin{pmatrix} 0 \\ -0.013 \\ 0 \end{pmatrix}$	3.7848
BB	50.9554	46.4287	1.2104	0	$\begin{pmatrix} 0.012 \\ 0.019 \\ 0 \end{pmatrix}$	$\begin{pmatrix} 0 \\ 0.013 \\ 0 \end{pmatrix}$	2.4171
TP	12.2677	28.4623	0.5366	0	$\begin{pmatrix} 0 \\ 0.046 \\ 0 \end{pmatrix}$	$\begin{pmatrix} 0.006 \\ -0.007 \\ 0 \end{pmatrix}$	1.1318
EMR	38.9908	12.3398	4.5431	13.3153	$\begin{pmatrix} 0 \\ 0.104 \\ 0 \end{pmatrix}$	$\begin{pmatrix} 0.008 \\ 0 \\ 0 \end{pmatrix}$	1.7460
FCU	48.4305	8.2307	1.1238	10.2369	$\begin{pmatrix} 0 \\ 0.164 \\ 0.01 \end{pmatrix}$	$\begin{pmatrix} -0.01 \\ 0 \\ 0.01 \end{pmatrix}$	1.3336
ECU	15.8504	9.0955	3.5109	0	$\begin{pmatrix} 0 \\ 0.0154 \\ -0.01 \end{pmatrix}$	$\begin{pmatrix} 0 \\ 0.004 \\ -0.01 \end{pmatrix}$	0.4891

Bibliography

[1] *WakeOpColl at the cutting edge of formation flight!* URL: https://sites.uclouvain.be/wakeopcoll/node/293.

[2] Victor Colognesi, Renaud Ronsse, and Philippe Chatelain. "Model coupling biomechanics and fluid dynamics for the simulation of controlled flapping flight". In: *Bioinspiration & Biomimetics* 16.2 (Feb. 2021). PMID: 33470974. DOI: 10.1088/1748-3190/abdd9c. URL: https://doi.org/10.1088/1748-3190/abdd9c.

[3] *File:Wing Muscles, color.svg - Wikimedia Commons*. URL: https://commons.wikimedia.org/wiki/File:Wing_Muscles,_color.svg.

[4] Douglas L. Altshuler et al. "The biophysics of bird flight: functional relationships integrate aerodynamics, morphology, kinematics, muscles, and sensors". In: *Canadian Journal of Zoology* 93.12 (2015), pp. 961–975. DOI: 10.1139/cjz-2015-0103.

[5] Guillaume Lamine. "Musculoskeletal modelling of the bird". MA thesis. EPL, Université catholique de Louvain, 2018.

[6] C. J. Pennycuick, Holliday H. Obrecht, and Mark R. Fuller. "Empirical estimates of body drag of large waterfowl and raptors." In: *Journal of Experimental Biology* 135 (Oct. 1988), pp. 253–264. DOI: 10.1242/jeb.135.1.253.

[7] Philip C. Withers. "AN AERODYNAMIC ANALYSIS OF BIRD WINGSAS FIXED AEROFOILS". In: *Journal of Experimental Biology* 90 (1981), pp. 143–162.

[8] Florian Muijres et al. "Comparative aerodynamic performance of flapping flight in two bat species using time-resolved wake visualization". In: *Journal of the Royal Society, Interface / the Royal Society* 8 (Mar. 2011), pp. 1418–28. DOI: 10.1098/rsif.2011.0015.

[9] F.E. Zajac. "Muscle and tendon: properties, models, scaling, and application to biomechanics and motor control". In: *Critical Reviews in Biomedical Engineering* 17 (Jan. 1989). PMID: 2676342, pp. 359–411.

[10] Thomas J. Roberts et al. "The Multi-Scale, Three-Dimensional Nature of Skeletal Muscle Contraction". In: *Physiology* 34.6 (2019). PMID: 31577172, pp. 402–408. DOI: 10.1152/physiol.00023.2019.

[11] Carolyn M., Emanuel Azizi, and Thomas J. Roberts. "Structural Determinants of Muscle Gearing During Dynamic Contractions". In: *Integrative and Comparative Biology* 58 (Aug. 2018), pp. 207–218. DOI: 10.1093/icb/icy054.

[12] Alexandra Hamburger. “Comparison between different muscular models”. MA thesis. EPL, Université catholique de Louvain, 2017.

[13] Hartmut Geyer and Hugh Herr. “A Muscle-Reflex Model That Encodes Principles of Legged Mechanics Produces Human Walking Dynamics and Muscle Activities”. In: *IEEE Transactions on Neural Systems and Rehabilitation Engineering* 18 (Apr. 2010), pp. 263–273. DOI: 10.1109/TNSRE.2010.2047592.

[14] Bhargava LJ, Pandy MG, and Anderson FC. “A phenomenological model for estimating metabolic energy consumption in muscle contraction”. In: *Journal of Biomechanics* 37 (Apr. 2004), pp. 81–88. DOI: 10.1016/S0021-9290(03)00239-2.

[15] B Umberger, Gerritsen K, and Martin P. “A model of human muscle energy expenditure”. In: *Comput Methods Biomech Biomed Engin.* 6 (Apr. 2003), pp. 99–111. DOI: 10.1080/1025584031000091678.

[16] Y. Yang, H. Wang, and Z. Zhang. “Muscle architecture of the forelimb of the Golden Pheasant (Chrysolophus pictus) (Aves: Phasianidae) and its implications for functional capacity in flight”. In: *Avian Research* 6 (Mar. 2015). DOI: 10.1186/s40657-015-0013-2.

[17] Winters JM. “An improved muscle-reflex actuator for use in large-scale neuromusculoskeletal models”. In: *Annals of Biomedical Engineering* 23 (Apr. 1995), pp. 359–374.

[18] Florian Michaud. “Neuromusculoskeletal human multibody models for the gait of healthy and spinal-cord-injured subjects”. PhD thesis. Universidade da Coruña, 2019.

[19] Nicolas Van der Noot. “Rich and robust bio-inspired locomotion control for humanoid robots”. PhD thesis. EPL, Université catholique de Louvain, Aug. 2017.

[20] URL: https://www.internationalairportreview.com/news/34612/robotic-bird/.

[21] URL: https://www.google.com/search?q=raie+poisson&hl=fr&source=lnms&tbm=isch&sa=X&ved=2ahUKEwjF1vPVyJTxAhVM8OAKHYjlCUcQ_AUoAXoECAEQAw&biw=1408&bih=678#imgrc=W1P0gXD2pHt6XM.

[22] URL: https://fr.wikipedia.org/wiki/Myliobatiformes.

[23] URL: https://pixnio.com/fr/faune-animaux/insectes-et-bugs/abeilles-insectes-photos/abeille-nature-fleur-la-pollinisation-pollen-insectes-abeilles.

[24] James R. Usherwood et al. “High aerodynamic lift from the tail reduces drag in gliding raptors”. In: *Comparative biomechanics of movement* (Feb. 2020). DOI: 10.1242/jeb.214809.

[25] nature video. *Birds gliding through bubbles reveal aerodynamic trick*. URL: https://www.internationalairportreview.com/news/34612/robotic-bird/.

[26] URL: https://en.wikipedia.org/wiki/Northern_bald_ibis.

UNIVERSITÉ CATHOLIQUE DE LOUVAIN
École polytechnique de Louvain
Rue Archimède, 1 bte L6.11.01, 1348 Louvain-la-Neuve, Belgique | **www.uclouvain.be/epl**